

Well balanced residual distribution for the ALE spherical shallow water equations on moving adaptive meshes

Luca Arpaia and Mario Ricchiuto

*Coastal Risk and Climate Change Unit, French Geological Survey
3 Av. C. Guillaumin 45060 Orléans Cedex 2, France
and
Team CARDAMOM, Inria Bordeaux Sud-Ouest,
200 av. de la vieille tour, 33405 Talence cedex, France*

Abstract

We consider the numerical approximation of the Shallow Water Equations (SWEs) in spherical geometry for oceanographic applications. To provide enhanced resolution of moving fronts present in the flow we consider adaptive discrete approximations on moving triangulations of the sphere. To this end, we restate all Arbitrary Lagrangian Eulerian (ALE) transport formulas, as well as the volume transformation laws, for a 2D manifold. Using these results, we write the set of ALE-SWEs on the sphere. We then propose a Residual Distribution discrete approximation of the governing equations. Classical properties as the DGCL and the C-property (well balancedness) are reformulated in this more general context. An adaptive mesh movement strategy is proposed. The discrete framework obtained is thoroughly tested on standard benchmarks in large scale oceanography to prove their potential as well as the advantage brought by the adaptive mesh movement.

Keywords: Shallow Water equations; curvilinear coordinates; Arbitrary Lagrangian Eulerian formulation; Moving Mesh ; Residual Distribution; Well-Balanced

1. Introduction

sec:intro

The Earth's curvature has a strong impact on wave propagation at large scales. For this reason, efficient and accurate techniques to solve flow equations on the sphere are of interest in many fields, such as ocean modeling, weather prediction as well as coastal hazards. Our objective is to explore the possibility of improving the discrete resolution of flows relevant to large-scale oceanographic applications by adaptively deforming an initial mesh, possibly already adapted to some of the data (e.g. initial depth or depth

Email address: l.arpaia@brgm.fr, mario.ricchiuto@inria.fr (Luca Arpaia and Mario Ricchiuto)

7 at rest). Indeed, mesh adaptation is useful to handle not only complex wave patterns, but also complex
8 bathymetries and coastlines. In this respect, the possibility of working on triangular grids may be useful
9 especially when approaching shallow areas. On these triangulations, in the spirit of the work done in
10 [ArR:17](#), we aim to assess the potential of adaptive mesh deformation, as well as its limitations for complex
11 multi-scale computations.

12
13 To achieve this objective, there are several aspects to be dealt with. The first one is the discrete
14 formulation of the Shallow Water Equations (SWEs) on the sphere. The literature on the topic is quite
15 large. On structured quadrilateral grids, it is common to formulate the SWEs in covariant curvilinear
16 coordinates (with the set of covariant coordinates identified by a patchwise parametrization of the sphere).
17 In the finite volume context, a thorough analysis is discussed in [Ros:04,Ros:06](#) and other formulations are proposed
18 e.g. in [UlJ:10,Cas:18](#). On triangular meshes most works focus on high order local finite element-like mappings as
19 in e.g. [Comb:09,Bern:09](#), or on a fully 3D formulation with Lagrange multipliers to locally re-project vectors on the
20 appropriate basis. A compromise is the initial work of [Ros:13](#), in which covariant coordinates are combined
21 with triangular grids and with a Residual Distribution (RD) discretization. An *ad-hoc* patching at the
22 poles guarantees the C^0 continuity of the solution. This provides us with an initial framework to extend
23 our previous work. In particular, we have shown in [RiB:09,r11,Ric:15](#) that RD method allows to handle very
24 naturally source terms with a simple design of schemes preserving many known steady equilibria on un-
25 structured triangulations. This is relevant when considering the SWEs in curvilinear coordinates which
26 embed several geometrical and physical forcing terms. The RD method also allows to combine high order
27 with monotonicity and positivity preservation principles. The work of [Ros:13](#) however is limited to steady
28 state problems, on fixed grids, with constant bathymetry, and linear schemes. Here we present a more
29 general development of nonlinear second order discrete approximations, for steady and time dependent
30 problems on complex bathymetries.

31
32 Another important aspect is the design of the adaptation strategy on the sphere. The geophysics
33 community has focused on quad-tree AMR techniques based on cell subdivision, see for example [SkK:92](#)
34 or [McU:15,Fer:16](#) [LGB:11,Pop:11](#)
35 or [\[13, 14\]](#), and [\[15, 16\]](#) for tsunami propagation. Here we consider a different approach, consisting
36 in generating an initial grid adapted to the problem's data (e.g. topography) and then using mesh
37 deformation to track more accurately the flow features. An elegant way to deal with the underlying moving
38 framework attached to the grid, see the original work of [HIRT1974](#) [ZS:03,KSD:12,Zho:13,ArR:17](#)
39 and [\[17, 18, 19, 20, 1\]](#) for application in geophysics.

39 Given an ALE map $x = A(X, t)$ between a reference (fixed) domain and an actual (moving) one, there
40 are two ways to formulate the PDEs in ALE form: either with respect to the reference coordinates X
41 or the actual ones x . In the former case, the derivation of the ALE equations in the reference domain
42 becomes immediate in a spacetime setting: the transformation of the 4-divergence differential operator
43 under the ALE map introduces an additional ALE transport term. An overview of the fundamental
44 relations necessary to achieve this in a spacetime setting are discussed in e.g. [\[21\]](#) (or chapter 2 in
45 the book [\[22\]](#)), see [\[19\]](#) for applications in geophysics, and [\[23, 24, 25, 26\]](#) for finite volume/element
46 formulations on curved meshes based on similar principles. There is certainly a similarity in the use of
47 the reference coordinates X to represent the mesh movement and the aforementioned use of curvilinear
48 coordinates to represent a geometrical manifold. Such analogy between the ALE form of balance laws and
49 e.g. the governing equations of relativistic hydrodynamics, which are written in a time-dependent curved
50 spacetime, is discussed in [\[27\]](#).

51 In moving mesh applications, another strategy used very often is to express the differential operators
52 in the actual configuration, and thus discretize them on the actual (moving) mesh. Within such approach,
53 a special role is played by the Geometric Conservation Law (GCL), which enforces conservation of the
54 total volume of the moving domain [\[ThL:79, LeF:96, GuF:00:79\]](#) [\[28, 29, 30\]](#). In [\[28\]](#) it was proposed to replace the GCL with the
55 constraint of reproducing exactly uniform flows, and in [\[30\]](#) it has been shown that satisfying the Geometric
56 Conservation Law (GCL) is a sufficient condition for first order time accuracy on moving meshes. The
57 compliance of the GCL at a discrete level is referred to as Discrete GCL (DGCL). Although rooted in
58 fundamental relations of continuous mechanics [\[Ba08, CFSI12\]](#) [\[21, 22\]](#), the practical importance/benefit of the GCL and
59 of its discrete counterpart is sometimes controversial, see e.g. [\[Eti:09\]](#) [\[31\]](#).

60 The approach that we use is of mixed type [\[SaA:08\]](#) [\[32\]](#). The spherical map is written with respect to the
61 curvilinear covariant coordinates. This means that the parametrization of the sphere is embedded in the
62 PDE system with the appropriate metric and source terms as in e.g. [\[Ros:04, Ros:06, UlJ:10, Ros:13, Cas:18\]](#)
63 [\[2, 3, 4, 8, 5\]](#). The ALE map, on
64 the contrary is written in the actual configuration, which does not require the computation of the ALE
65 Jacobian matrix. In this setting, the ALE-SWEs on a 2D manifold will be derived using classical transport
66 formulas and volume conservation statement. A derivation of the governing equations in spacetime is also
67 given in the Appendix. It will be shown that, for the SWEs on the sphere, the satisfaction of a DGCL
68 is a necessary condition to retain well-balancedness. To this end, a new ALE closure for RD schemes is
69 proposed, since the one of [\[ArR:14\]](#) [\[33\]](#) does not extend to the sphere, and more in general to manifolds.

70 The schemes obtained are thoroughly tested both on fixed and moving adaptive meshes on classical

71 applications for the shallow water on the sphere, and on a realistic computation of relevance in oceanog-
 72 raphy: the regional propagation and coastal impact of the 2011 Tohoku-Honsu tsunami.

73

74 The paper is organized as follows. The standard SWEs **in spherical geometry** are recalled in section
 75 ~~2.~~ Sections ~~3~~ and ~~4~~ are then devoted to the ALE-SWEs formulation **on the sphere**. The main notation
 76 and ingredients required for the discrete approximation are the introduced in section ~~5.~~ ^{eq: not-as} These are used in
 77 section ~~6~~ ^{sec: RD} to construct well balanced second order residual distribution. The mesh movement strategy is
 78 discussed in section ~~7,~~ ^{sec: mmpde} and section ~~8~~ ^{sec: exp} discusses an extensive evaluation of the schemes. The paper is ended
 79 by a summary and an outlook on future developments.

80 2. SWEs on the sphere

sec:SW-sphere

In this section we recall the Shallow Water Equations (SWEs) on the sphere in covariant curvilinear coordinates. At every point of the sphere \mathcal{S}^2 we fix an orthogonal but not orthonormal reference system with covariant basis vectors $\{\mathbf{g}_1, \mathbf{g}_2\}$ together with local curvilinear coordinates $\{x^1, x^2\}$. The vectors \mathbf{g}_1 and \mathbf{g}_2 define the tangent plane to the sphere and are used to construct all quantities allowing to locally describe the manifold. For completeness, in ^{app: a1.1} Appendix A.1 we recall some basic concepts from differential geometry, as well as many definitions used throughout the following sections. We will consider the evolution of the fluid depth $h(\mathbf{x}, t)$ measured along the radial axis. The bathymetry/topography height with respect to a given reference level is denoted by $b(\mathbf{x})$. The fluid free surface is defined here as $\eta = h + b$. We denote hu^i the components of the discharge vector $hu = hu^i \mathbf{g}_i$. We remark that the velocity components are not defined in a unitary basis. The SWEs in covariant curvilinear coordinates write¹:

$$\begin{aligned} \frac{\partial h}{\partial t} + \frac{1}{\sqrt{G}} \frac{\partial}{\partial x^j} \left(\sqrt{G} hu^j \right) &= 0 \\ \frac{\partial hu^i}{\partial t} + \frac{1}{\sqrt{G}} \frac{\partial}{\partial x^j} \left(\sqrt{G} T^{ij} \right) + S^i &= 0 \end{aligned} \quad (1) \quad \text{eq: SW-s}$$

81 G denotes the determinant of the metric tensor defined in ^{eq: Gij def: a1} (A.3) in Appendix A, and $T^{ij} = hu^i hu^j + \frac{1}{2} G^{ij} gh^2$
 82 are the components of the momentum flux $\mathbf{T} = T^{ij} \mathbf{g}_i \mathbf{g}_j$, involving the components of the inverse metric
 83 tensor, also defined in the appendix.

The source term in the momentum balance reads

$$S^i = G^{ij} gh \frac{\partial b}{\partial x^j} + c_F hu^i + S_\gamma^i - S_c^i \quad (2)$$

¹standard summation convention is used, for the notation we refer again to ^{app: a1} Appendix A

Besides the effects of bathymetry and friction (first two terms), the source includes also a geometrical force due to Earth curvature S_γ^i , and Coriolis term S_c^i . The geometric source arises from the space variation of the covariant basis vectors and reads

$$S_\gamma^i = \Gamma_{jk}^i T^{jk} \quad (3)$$

with Γ_{jk}^i being the Christoffel symbols. The Coriolis term is associated to the rotation of the Earth, which plays an important role in ocean dynamics. It reads

$$S_c^i = fG^{ij}\varepsilon_{jk}hu^k \quad (4)$$

84 with the parameter $f = 2\Omega \sin \lambda$ with λ the latitude and Ω the Earth rotation rate, always taken as
 85 $\Omega = 7.292 \times 10^{-5} \text{ s}^{-1}$ unless differently specified, and having denoted by ε the 2D Levi-Civita symbol.

86 The SWEs system can also be expressed in a compact vector form

$$\frac{\partial \mathbf{u}}{\partial t} + \frac{1}{\sqrt{G}} \frac{\partial \mathbf{F}^j}{\partial x^j} + \mathcal{S}(\mathbf{x}, \mathbf{u}) = 0, \quad (5)$$

$$\mathbf{u} = \begin{bmatrix} h \\ hu^i \end{bmatrix}, \quad \mathbf{F}^j = \sqrt{G} \begin{bmatrix} hu^j \\ T^{ij} \end{bmatrix}, \quad (6)$$

$$\mathcal{S} = \underbrace{\begin{bmatrix} 0 \\ G^{ij}gh \frac{\partial b}{\partial x^j} \end{bmatrix}}_{S^b} + \underbrace{\begin{bmatrix} 0 \\ c_F hu^i \end{bmatrix}}_{S^f} + \underbrace{\begin{bmatrix} 0 \\ \Gamma_{jk}^i T^{jk} \end{bmatrix}}_{S^\gamma} - \underbrace{\begin{bmatrix} 0 \\ fG^{ij}\varepsilon_{jk}hu^k \end{bmatrix}}_{S^c} \quad (7)$$

87 Equations (5)-(7) constitute a non-homogeneous hyperbolic system of PDEs. As in [34] we remark that
 88 the flux vector depends explicitly on the position making the system non-autonomous.

3. Arbitrary Lagrangian Eulerian framework on the sphere

89 sec:ale

We now introduce an independent configuration \mathcal{A} , the Arbitrary Lagrangian Eulerian (ALE) configuration, which we assume to belong to a differentiable manifold (the sphere). For us \mathcal{A} will be the configuration the mesh is attached to. \mathcal{A} is composed of points Q identified by the vector \mathbf{x} which can be expressed in the local curvilinear coordinate system $\mathbf{x}(Q) = x^i \mathbf{g}_i$, with $i = 1, 2$. The initial or *reference* configuration of the continuous mesh is denoted by \mathcal{A}_0 and the reference position of the points is denoted by greek letters $\chi(\hat{Q})$. For this configuration we assign a local covariant vector basis $\{\gamma_1, \gamma_2\}$ and local chart $\{\chi^1, \chi^2\}$ of the tangent plane so that $\chi(\hat{Q}) = \chi^i \gamma_i$. As the mesh moves, also \mathcal{A} does. We assume to be able to uniquely map the initial configuration to the reference one via the mapping:

$$A : \mathcal{A}_0 \rightarrow \mathcal{A} \quad \mathbf{x} = A(\chi, t) \quad (8)$$

90 The function A is assumed to be continuously differentiable, with a smooth Jacobian $\mathbf{J}_A = \frac{\partial \mathbf{x}}{\partial \mathbf{X}}$. Classical
 91 requirements on the Jacobian \mathbf{J}_A are invertibility $\exists \mathbf{J}_A^{-1}$, and the positivity of its determinant $J_A =$
 92 $\det \mathbf{J}_A > 0$. For a spacetime definition of the ALE transformation see (Appendix A.2).

The fluid is endowed with various physical properties which may be represented by scalar, vector and tensor fields. These fields and their rate of change in time and space may be defined in the reference configuration or in the actual one. Here we choose the actual description: that is, in the following, all spatial derivatives are expressed with respect to the actual coordinates. The ALE time derivative of a scalar ϕ is its time rate of change measured by an observer which moves with the mesh point labeled with χ , where $\chi(\hat{Q})$ is the particle's position in the reference configuration. We will shorten it $\left. \frac{\partial \phi}{\partial t} \right|_{\chi}$. The ALE/mesh velocity of a point Q in the actual vector basis, $\boldsymbol{\sigma}(Q) = \sigma^j \mathbf{g}_j$ is calculated by applying the aforementioned definition of ALE derivative, to the position $\mathbf{x}(Q)$. Its components write

$$\sigma^j = \left. \frac{\partial x^j}{\partial t} \right|_{\chi} \quad (9)$$

93 Using chain rule, we can define relations between Eulerian and ALE time derivatives for these properties:

$$\left. \frac{\partial \phi}{\partial t} \right|_{\chi} = \frac{\partial \phi}{\partial t} + \frac{\partial \phi}{\partial x^j} \sigma^j \quad (10)$$

Finally, taking the ALE time derivative of an infinitesimal area on the sphere we obtain the Geometric Conservation Law on the manifold ^{[tru:66} [35]:

$$\left. \frac{\partial}{\partial t} \right|_{\chi} (\sqrt{G} J_A) = J_A \frac{\partial}{\partial x^j} (\sqrt{G} \sigma^j) \quad (11) \quad \boxed{\text{eq:gcl-s}}$$

94 or, more compactly $\left. \partial_t \right|_{\chi} (\sqrt{G} J_A) - J_A \sqrt{G} \nabla \cdot \boldsymbol{\sigma} = 0$.

95 The GCL (II) ^{eq:gcl-s} is a geometrical relation between the ALE Jacobian and the ALE velocity. One can
 96 check that the integral of (III) ^{eq:gcl-s} over the whole computational domain states the conservation of the total
 97 area. At a discrete level this corresponds to preserve the total area of the mesh during the simulation.
 98 For this reason in section ^{sec:dgcl-s} 5.3 we will discuss how to preserve also its discrete counterpart.

99 4. ALE-SWEs on the sphere

ale-SW-sphere
 100 Using the relations derived in the previous sections, and more particularly (II) ^{eq:tra-a} and (III) ^{eq:gcl-s}, we can easily
 101 recast the SWEs (I) ^{eq:SW-s} in an ALE form, obtaining the ALE-SWEs on a 2D manifold with respect to the

102 actual parametric coordinates:

$$\frac{\partial \sqrt{G} J_A h}{\partial t} \Big|_{\mathbf{x}} + J_A \frac{\partial}{\partial x^j} \left(\sqrt{G} h u^j - \sqrt{G} h \sigma^j \right) = 0 \quad (12)$$

$$\frac{\partial \sqrt{G} J_A h u^i}{\partial t} \Big|_{\mathbf{x}} + J_A \frac{\partial}{\partial x^j} \left(\sqrt{G} T^{ij} - \sqrt{G} h u^i \sigma^j \right) + \sqrt{G} J_A S^i = 0 \quad (13)$$

103 As before, the system can be also cast in compact vector form as

$$\frac{\partial}{\partial t} \Big|_{\mathbf{x}} \left(\sqrt{G} J_A \mathbf{u} \right) + J_A \frac{\partial}{\partial x^j} \left(\mathbf{F}^j - \sqrt{G} \sigma^j \mathbf{u} \right) + \sqrt{G} J_A \mathcal{S}(\mathbf{x}, \mathbf{u}) = 0 \quad (14)$$

Finally, it is useful for the following to recall that the bathymetry, which does not depends explicitly on time $b = b(\mathbf{x})$, verifies the following identity:

$$\frac{\partial b}{\partial t} \Big|_{\mathbf{x}} = \frac{\partial b}{\partial x^j} \sigma^j \quad (15)$$

104 multiplying by $J_A \sqrt{G}$ and summing it to the GCL (II1) (multiplied by b) we obtain the ALE remap on the 2D manifold

$$\frac{\partial \sqrt{G} J_A b}{\partial t} \Big|_{\mathbf{x}} - J_A \frac{\partial}{\partial x^j} \left(\sqrt{G} b \sigma^j \right) = 0 \quad (16)$$

eq:b_ALE_remap

105 Please note that scalar, vector, tensor fields and spatial derivatives are written w.r.t. the actual coordinates \mathbf{x} , in all the expressions above. For completeness in (app:a2) (Appendix B) we report an alternative derivation of the governing equations (II4) with a spacetime approach.

107 5. Discretization: parametrization and constraints

eq:not-as

108 In this section we discuss the basic aspects of the discretization. These involve the main geometrical notations as well as the form of the equation used for the discretization. We will introduce an appropriate form of the ALE-SWEs allowing to combine well-balancedness with geometric conservation. We then show how to embed discrete analogs of these constraints in a residual distribution setting.

112 5.1. Unstructured grid representations: main notation

113 Points on a manifold are represented by a proper parametrization through the use of geometrical mappings. In particular, when working in ALE formalism, a point i will be expressed in the parametrization of the initial configuration by a vector $\boldsymbol{\chi}_i = \{\chi^1, \chi^2\}_i$, while $\mathbf{x}_i = \{x^1, x^2\}_i$ will refer to the configuration attached to the mesh. Note that the discussion here is general, even though the numerical applications will only consider a latitude longitude parametrization of the sphere. This particular choice is known

118 to introduce a singularity at the poles, which is nowadays well handled by meteorologists ^{Wil:07}[36]. Since we
 119 are interested in oceanic applications we circumvent this issue by adopting a simple fix. A patch-wise
 120 parametrization of the sphere (see e.g. ^{KaS:04:96}[37][38] and references therein) is deployed, namely a polar cap
 121 defined by a limiting latitude λ_{lim} , in which we use a rotated reference system $(x', y', z') = (x, z, -y)$. To
 122 account for this "patching", a rotation operator needs to be applied when updating vectors in elements
 123 crossing the patch boundary. In our case, this applies both to physical velocities, as well as mesh nodes
 124 velocities and position. In all right hand side evaluations this is accounted for following ^{Ros:13}[8] to which we
 125 refer for details.

We consider a discretization of \mathcal{S}^2 composed by non overlapping triangular elements \mathcal{K} . To each element \mathcal{K} we can associate an element defined in the parametric space, which we denote by K . For each element, we define the spherical area and median dual cell of a node as

$$|\mathcal{K}(t)| = \int_{K(t)} \sqrt{G} d\mathbf{x}, \quad |C_i| = \sum_{K \in \mathcal{D}_i} \frac{|\mathcal{K}|}{3} \quad (17) \quad \text{eq:sp-tr}$$

For moving meshes we also have:

$$|\mathcal{K}(t)| = \int_{K_0} J_A(t) \sqrt{G} d\boldsymbol{\chi}. \quad (18) \quad \text{eq:sp-tr-ALE}$$

126 denoting by K_0 the element in the initial parametric space. Please note that, after the change of coor-
 127 dinates, we assume in the above expression that $\sqrt{G(\boldsymbol{\chi}(t))}$. This duality of integral formulas via the
 128 ALE mapping applies to all integrals and will not be recalled explicitly unless necessary.

For a given mesh, we label by h the largest element diameter in the parameter space M^2 . For a smooth enough initial mesh, and on a smooth manifold, we unduly assume that the number of elements N_K verifies

$$N_K |K| \leq c |M^2| \quad (19) \quad \text{eq:mesh-smooth}$$

for some bounded constant. We also denote by \mathbf{u}_h the P^1 approximation of a quantity \mathbf{u}

$$\mathbf{u}_h(\mathbf{x}) = \sum_i \mathbf{u}_i \varphi_i(\mathbf{x}) \quad (20) \quad \text{eq:fem}$$

having denoted by φ_i the standard P^1 bases. We now define elemental contributions to the Galerkin mass matrix

$$(m_{ij}^{GAL})^K := \int_K \varphi_i \varphi_j \sqrt{G}(\mathbf{x}) d\mathbf{x}, \quad (21) \quad \text{eq:gal-mass}$$

as well as to the lumped mass matrix

$$(m_{ij}^{GAL})^{L,K} := \mathcal{K}_i \delta_{ij}, \quad \mathcal{K}_i := \int_K \sqrt{G}(\mathbf{x}) \varphi_i d\mathbf{x}. \quad (22) \quad \text{eq:gal-mass-L}$$

5.2. Well-Balancedness and GCL on the sphere

For shallow water flows, a very important role is played by the lake-at-rest steady state:

$$h\mathbf{u} = 0, \quad h + b = \eta_0 = \text{const} \quad (23)$$

eq:lake_at_res

The exact preservation of this (initial) steady state at the discrete level is referred to as the *C-property*, or *Well-Balancedness* ^{BeV:94} [39]. In other words, well-balanced schemes provide a discrete analog of the balance (cf. equation ^{eq:SW-sph} (5))

$$\frac{\partial \mathbf{F}^j}{\partial x^j} + \sqrt{G} \mathcal{S} = 0. \quad (24)$$

Written in the form ^{eq:SW1-as} (II4), the ALE-SWEs require the simultaneous satisfaction of several compatibility constraints in order to devise well-balanced schemes. These constraints include:

1. well-balancedness for the Cartesian SWEs on fixed grids: $\partial_{x^i}(gh^2/2) + gh\partial_{x^i}b = 0, \forall i$;
2. a discrete analog of the GCL on moving grids ^{eq:gcl-s} (II1);
3. the ALE remap of the bathymetry ^{eq:b_ALE_remap} (II6);
4. the metric relations ^{eq:Ric} (A.6) given in ^{app:a1} (Appendix A);

We will show in the following of the paper how we can embed *exactly* the first two constraints at a discrete level. Concerning the third, replacing $\mathbf{u} = 0$ in the first of ^{eq:SW1-as} (II4) we get

$$\begin{aligned} 0 &= \left. \partial_t(\sqrt{G} J_A h) \right|_x - J_A \partial_{x^j}(\sqrt{G} \sigma^j h) \\ &= \left. \partial_t(\sqrt{G} J_A \eta) \right|_x - J_A \partial_{x^j}(\sqrt{G} \sigma^j \eta) - \left[\left. \partial_t(\sqrt{G} J_A b) \right|_x - J_A \partial_{x^j}(\sqrt{G} \sigma^j b) \right] \end{aligned} \quad (25)$$

If $\eta = \eta_0$ we see that a necessary condition for the lake-at-rest to be a solution for system ^{eq:SW1-as} (II4) is to verify *both* the GCL, and the ALE remap of the bathymetry. Some authors ^{ZhC:13} [40] have proposed to directly use a discretization of ^{eq:b_ALE_remap} (II6) to evolve the topography on a moving mesh. The drawback of this approach is that it significantly modifies the bathymetry during the computation, which cannot be accepted in practical applications. For this reason, here we follow ^{ArR:17} [1] and modify ^{eq:SW1-as} (II4) by solving instead the system obtained by adding to the first equation the ALE remap of the bathymetry:

$$\frac{\partial}{\partial t} \Big|_x \left(\sqrt{G} J_A \mathbf{w} \right) + J_A \frac{\partial}{\partial x^j} \left(\mathbf{F}^j - \sqrt{G} \sigma^j \mathbf{w} \right) + \sqrt{G} J_A \mathcal{S}(\mathbf{x}, \mathbf{u}) = 0, \quad \mathbf{w} = \begin{bmatrix} \eta \\ h\mathbf{u} \end{bmatrix} \quad (26)$$

eq:SW-aswb

Note that, with this notation, we have $\mathbf{F}^j(\mathbf{u}) = \mathbf{F}^j(\mathbf{w}; b)$, as the bathymetry is required to evaluate the flux starting from the \mathbf{w} array. Concerning now the fourth requirement, we consider the momentum balance

obtained when replacing the lake-at-rest solution in (26).^{eq:SW-aswb} Setting $\Pi = gh^2/2$ for short, we have

$$\begin{aligned} 0 &= J_A \left\{ \partial_{x^j} (\sqrt{G} G^{ij} \Pi) + \sqrt{G} \Gamma_{jk}^i G^{jk} \Pi + gh \sqrt{G} G^{ij} \partial_{x^j} b \right\} \\ &= J_A \left\{ \sqrt{G} G^{ij} (gh \partial_{x^j} b + \partial_{x^j} \Pi) + \Pi \left[\partial_{x^j} (\sqrt{G} G^{ij}) + \sqrt{G} \Gamma_{jk}^i G^{jk} \right] \right\} \end{aligned} \quad (27) \quad \text{eq:wbs}$$

The first group in parentheses vanishes if the first property (well-balancedness for Cartesian SWEs on fixed grids) is satisfied. The remainder is nothing else than the combination of the two metric relations. Indeed just by replacing the second relation of (A.6)^{eq:Ric} into Ricci's Lemma we obtain

$$\begin{aligned} 0 &= \sqrt{G} \left(\frac{\partial G^{ij}}{\partial x^j} + G^{ij} \Gamma_{mj}^m + \Gamma_{jm}^i G^{mj} \right) \\ &= \sqrt{G} \frac{\partial G^{ij}}{\partial x^j} + G^{ij} \frac{\partial \sqrt{G}}{\partial x^j} + \sqrt{G} \Gamma_{jm}^i G^{mj} = \frac{\partial \sqrt{G} G^{ij}}{\partial x^j} + \sqrt{G} \Gamma_{jm}^i G^{mj} \end{aligned} \quad (28)$$

The symmetry of the Christoffel symbols [41]^{Ngu:14} allows to recover exactly the last expression in parentheses in (27).^{eq:wbs} The above relation is thus necessary for the lake-at-rest solution to be verified. At the discrete level, the easiest way to make sure this condition is embedded is to combine high order quadrature with the direct use of the analytical formulas. Even though low quadrature errors can be obtained with relatively few quadrature points, due to the smoothness of the functions involved, in this way the C-property would be satisfied within this quadrature error. Also, compared to the Cartesian case, the necessity of using higher order quadrature would still give a considerable overhead. For this reason we have chosen to embed the metric relations analytically. Whenever possible we discretize the momentum balance in the following form:

$$\begin{aligned} \frac{\partial}{\partial t} \Big|_x \left(\sqrt{G} J_A h u^i \right) + J_A \frac{\partial}{\partial x^j} \left(\sqrt{G} h u^i (u^j - \sigma^j) \right) + J_A \sqrt{G} G^{ij} \left(\frac{\partial}{\partial x^j} (gh^2/2) + gh \frac{\partial}{\partial x^j} b \right) \\ + J_A \sqrt{G} S^i = 0. \end{aligned} \quad (29) \quad \text{eq:qdm-wb}$$

For later use in the paper, we introduce the short notation

$$\frac{\partial (J_A \sqrt{G} \mathbf{w})}{\partial t} \Big|_x + J_A \mathcal{R}(\mathbf{w}, b) = 0 \quad (30) \quad \text{eq:ut_lu}$$

136 for the system obtained with the first in (26), plus (29).^{eq:SW-aswb eq:qdm-wb}

137 5.3. DGCL on the sphere

138 We consider now the satisfaction of the discrete analog of the GCL on a 2D manifold (II).^{eq:gcl-s} As already
139 said, differently from the Cartesian case, a uniform flow is not an exact solution of (II4)^{eq:SW1-as} embedded with the
140 GCL (II1)^{eq:gcl-s}, even for constant bathymetries and in absence of friction and Coriolis force. As a consequence
141 we cannot define the DGCL through the original characterization of [28]^{ThL:79}, i.e. the preservation of a uniform

142 flow. On the sphere, we could replace the preservation of uniform flow with some other particular cases,
 143 as e.g. the preservation of zonal or meridional flows. However, the most relevant characterization of the
 144 GCL for the applications of this paper is the one we have introduced in the previous section, namely the
 145 satisfaction of the lake-at-rest state.

146 It is thus in the perspective of obtaining well balanced schemes on moving grids that we consider the
 147 issue of mimicking (II) at the discrete level. As we will shortly see, the main issue is properly defining the
 148 components of the mesh velocity σ^j along certain directions, as well as an approximation of the divergence
 149 operator $\partial_{x^j}(\sqrt{G}\sigma^j)$. The DGCL closure used in previous works by the authors [ArR:14, ArR:17
 150 [LeF:96, GuF:00
 [29, 30], is based on a piecewise linear P^1 interpolation of the mesh displacements. This definition allows to
 151 recover naturally an element-by-element DGCL when integrating the divergence of the displacements over
 152 the half time step average element $K^{n+1/2} = (K^{n+1} + K^n)/2$. Due to the presence of the coefficient \sqrt{G} ,
 153 the extension of this approach is not at all straightforward. We have thus chosen to use a generalization
 154 of the closure originally proposed in [MaY:06
 [42].

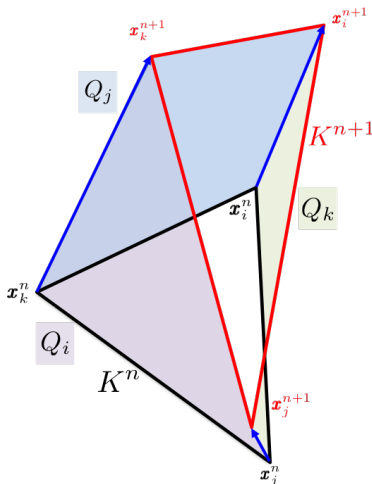


Figure 1: Swept area decomposition of area variations for mesh element K . fig:swept-area

To describe this closure, we consider an element \mathcal{K} of the mesh, or equivalently its projection in the parametric space K . We study the discrete approximation of the area variation

$$|\mathcal{K}^{n+1}| - |\mathcal{K}^n| = \left[\int_{K_0} J_A \sqrt{G} d\chi \right]^{n+1} - \left[\int_{K_0} J_A \sqrt{G} d\chi \right]^n$$

We decompose this variation in components associated to the area swept by each face, as illustrated in figure fig:swept-area. We have in particular

$$|\mathcal{K}^{n+1}| - |\mathcal{K}^n| = \Delta t \sum_{j \in K} v_{f_j}. \quad (31) \quad \text{eq:delta-K}$$

Denoting by Q_j the quadrilateral ($\{\mathbf{x}_i, \mathbf{x}_k\}^n; \{\mathbf{x}_i, \mathbf{x}_k\}^{n+1}$) (cf. figure [fig:swept-area](#) \square), v_{f_j} is the average edge velocity tangent to the manifold and normal to the edge defined by

$$v_{f_j} := \frac{1}{\Delta t} \int_{Q_j} \sqrt{G} d\mathbf{x} \quad (32) \quad \text{eq:ivc-s}$$

In practice, the integral is computed by a high order quadrature formula

$$\int_{Q_j} \sqrt{G} d\mathbf{x} = |Q_j| \sum_{\mathbf{x}_q} \omega_q \sqrt{G}(\mathbf{x}_q) \quad (33) \quad \text{eq:ivc-s1}$$

155 where the quadrature grid is built simply by tensorizing 1D quadrature points over each edge, and the
156 signed volume $|Q_j|$ is evaluated using the surveyor's (or shoelace) area formula [\[43\]](#).

157 To discretize the ALE-SWEs we now need to provide a discrete approximation of the curvilinear
158 divergence appearing in the GCL. For the purposes of the paper we would like this definition to be
159 compatible with the following relations

$$\mathcal{K}^{n+1} - \mathcal{K}^n = \int_{t^n}^{t^{n+1}} \int_{K_0} J_A \frac{\partial}{\partial x^j} (\sqrt{G} \sigma^j) \Big|_K d\boldsymbol{\chi} dt \quad (34)$$

$$\mathcal{K}_i^{n+1} - \mathcal{K}_i^n = \int_{t^n}^{t^{n+1}} \int_{K_0} J_A \varphi_i \frac{\partial}{\partial x^j} (\sqrt{G} \sigma^j) \Big|_K d\boldsymbol{\chi} dt \quad (35)$$

$$\int_{K_0} J_A^{n+1} \sqrt{G} \varphi_i \mathbf{w}_h - \int_{K_0} J_A^n \sqrt{G} \varphi_i \mathbf{w}_h = \int_{t^n}^{t^{n+1}} \int_{K_0} J_A \varphi_i \frac{\partial}{\partial x^j} (\sqrt{G} \sigma^j) \Big|_K \mathbf{w}_h d\boldsymbol{\chi} dt \quad (36)$$

160 with \mathbf{w}_h the approximation of the same data on the different meshes associated to the mappings with
161 Jacobians J_A^{n+1} and J_A^n . The first relation is the spacetime integral of the GCL while the second and the
162 third relations are useful to derive a consistent finite element method, and mass lumping. The practical
163 evaluation of each of the integrals on the left hand side plays here a fundamental role in our ability to
164 satisfy exactly the three relations above. We have the following characterization.

Proposition 1. (Approximate quadrature on the manifold and DGCL) *Consider a one point quadrature approximating the integral over a time step as*

$$\int_{t^n}^{t^{n+1}} \int_{K_0} J_A f(\boldsymbol{\chi}) d\boldsymbol{\chi} dt = \Delta t \int_{K_0} \bar{J}_A f(\boldsymbol{\chi}) d\boldsymbol{\chi} dt = \Delta t \int_{\bar{K}} f(\bar{\mathbf{x}}) d\bar{\mathbf{x}} dt$$

and the constant-by-element approximation of the divergence

$$\frac{\partial}{\partial x^j} (\sqrt{G} \sigma^j) \Big|_{\bar{K}} := \frac{1}{|\bar{K}|} \sum_{j \in \bar{K}} v_{f_j}. \quad (37) \quad \text{eq:div-dgcl}$$

Consider also the approximate quadrature defining full and lumped mass matrices (22) and (21) given by

$$(m_{ij}^{GAL})^K \approx \frac{|\mathcal{K}|}{3} \frac{1 + \delta_{ij}}{4}, \quad (m_{ij}^{GAL})^{L,K} = \mathcal{K}_i \delta_{ij} \approx \frac{|\mathcal{K}|}{3} \delta_{ij}. \quad (38)$$

eq:gal-mass-d

165 We have the following properties:

- 166 1. Relations (34), (35) and (36) are verified exactly;
- 167 2. For a smooth C^r function, with $r \geq 1$, if (19) is true, the projection associated to (38) is at least
168 second order accurate.

169 *Proof.* See (app:a3 (Appendix C)). □

170 **Remark 1.** (Higher order quadrature in mass matrices). The approximate quadrature (38) is only
171 required to embed exactly the GCL in the scheme. In absence of mesh movement, higher order (or exact)
172 quadrature can be used to define the mass matrix entries, which will differ from (38) within the quadrature
173 error just proved. In practice we have seen no advantage in using more accurate quadrature in these for-
174 mulas. For completeness, the modifications necessary to account (on fixed meshes) for the exact evaluation
175 of the mass matrices for Residual Distribution and stabilized finite elements are provided in (app:a4 (Appendix D)).
176

177 Note that in practice, when using the sphere with lat-lon parametrization, the gradient of \sqrt{G} appearing
178 in the error estimate in the appendix is given by $R^2 \sin \lambda$ with λ the latitude, which is clearly bounded.

179 Finally, note that the choice of \bar{J}_A is arbitrary and has no impact on the satisfaction of the DGCL. For
180 accuracy reasons, here we have kept a mid-point approximation $\bar{J}_A = (J_A^n + J_A^{n+1})/2$. This means that,
181 most geometrical quantities are evaluated as averages on the elements \mathcal{K}^{n+1} and \mathcal{K}^n . This is implicitly
182 assumed in all the formulas which will follow. For simplicity, in the text we will drop the superscript
183 altogether, unless necessary in the formula.

184 6. ALE Residual Distribution on the sphere

sec:RD

185 A first extension of Residual Distribution (RD) to general covariant coordinates has been proposed by
186 [8]. The work of the reference is limited to steady state computations, with linear schemes and without
187 bathymetry. This paper presents a general second order and well balanced formulation allowing time
188 dependent computations on moving meshes. The construction proposed here is a generalization of the
189 work done in Cartesian coordinates in [1]. We refer the interested reader to [44, 45] and references therein
190 for a thorough discussion of the properties of residual distribution.

The RD discretization of unsteady problems can be described starting with an analogy with stabilized continuous finite elements. Given a triangulation of the parametric domain S^2 , to solve $\mathcal{L}(\mathbf{w}_h) = 0$, one can formally recast a RD scheme as

$$\int_{S^2} w_i \mathcal{L}(\mathbf{w}_h) d\mathcal{X} = 0 \quad \text{eq:pg} \quad (39)$$

where $w_i = \varphi_i + \gamma_i$ is a Petrov-Galerkin test function, with γ_i an appropriately defined bubble function. For consistency, on each element K

$$\sum_{j \in K} w_j = 1, \quad \text{eq:rd-consiist} \quad (40)$$

which implies $\sum_j \gamma_j = 0$. We define the *element residual* associated to (26) as the area integral over the element of the full differential operator:

$$\Phi^K = \int_{K_0} \mathcal{L}(\mathbf{w}_h) d\mathcal{X}. \quad \text{eq:rd-consiist} \quad (41)$$

The consistency (40) allows to define the distributed residuals

$$\Phi_i^K := \int_{K_0} w_i \mathcal{L}(\mathbf{w}_h) d\mathcal{X} \quad \text{eq:rd-split0} \quad (42)$$

which verify the consistency condition

$$\sum_{j \in K} \Phi_j^K = \Phi^K. \quad \text{eq:rd-consiist} \quad (43)$$

In actual computations, the main component of the distributed residuals is evaluated by means of distribution matrices β_i^K which also verify consistency

$$\sum_{j \in K} \beta_j^K = 1. \quad \text{eq:rd-consiist} \quad (44)$$

The bridge with finite elements is completed by the requirement

$$\beta_i^K = \frac{1}{|K_0|} \int_{K_0} w_i d\mathcal{X} = \bar{w}_i^K. \quad \text{eq:rd-consiist} \quad (45)$$

which leads to form of the distribution used in practice:

$$\Phi_i^K = \beta_i^K \Phi^K + \int_{K_0} (w_i - \bar{w}_i^K) \mathcal{L}(\mathbf{w}_h) d\mathcal{X} \quad \text{eq:rd-split1} \quad (46)$$

191 The formula above shows the key design elements of the method which are the integration strategy used
 192 to evaluate Φ^K , and the definition of the distribution matrices and of the associated test functions. Note
 193 that the first term in the above formula is enough to have a consistent and conservative method (in the
 194 sense of (44)). The second term has an impact on the accuracy and stability, but none on consistency as
 195 clearly $\sum_j (w_j - \bar{w}_j^K) = 0$.

196

197 *6.1. Two-step explicit method*

198 Concerning the time marching technique, we consider here a fully explicit multi-stage strategy, relying
 199 on the ideas discussed in [\[46, 11\]](#). For recent implicit space-time strategies we refer to [\[47, 48, 49\]](#).

200 Concerning the scheme used here, we recall for completeness in [\(Appendix D\)](#) its construction which,
 201 starting from [\(39\)](#), relies on the following steps:

- 202 1. replacing $\mathcal{L}(w_h)$ by [\(30\)](#);
- 203 2. mapping integrals on the reference domain and their evaluation on the current configuration (mesh);
- 204 3. use of a simplified residual based stabilization involving an extrapolation of the time derivative;
- 205 4. use of Proposition 1, as well as of [\(34\)](#), [\(35\)](#), and [\(36\)](#);
- 206 5. lumping of the Galerkin mass-matrix.

In its final form, the scheme evolves nodal values of the state vector w with a two-step procedure, in which the new solution value is obtained from:

$$|\mathcal{C}_i^{n+1}|(w_i^{n+1} - w_i^*) = -\Delta t \sum_{K \ni i} \Phi_i^K \quad (47) \quad \boxed{\text{RC-corr}}$$

where the nodal residuals Φ_i^K are a splitting of the *element residual*

$$\sum_{j \in K} \Phi_j^K = \Phi^K = \frac{1}{\Delta t} \int_{K_0} (J_A^{n+1} \sqrt{G} w_h^* - J_A^n \sqrt{G} w_h^n) d\mathcal{X} + \frac{1}{2} \Phi^K(w_h^*, b_h^{n+1}) + \frac{1}{2} \Phi^K(w_h^n, b_h^n) \quad (48) \quad \boxed{\text{phi-corr}}$$

with $\Phi^K(w, b)$ the *fluctuation* (the area integral over the element K of only advective and source terms)

$$\begin{aligned} \Phi^K = \oint_{\partial K} \sqrt{G} \begin{bmatrix} hu^j - \eta \sigma^j \\ hu^i (u^j - \sigma^j) \end{bmatrix}_h n^j ds + \int_K \sqrt{G} \begin{bmatrix} 0 \\ G^{ij} (\partial_{x^j} (gh^2/2) + gh \partial_{x^j} b) \end{bmatrix}_h d\mathbf{x} \\ + \int_K \sqrt{G} \begin{bmatrix} 0 \\ \mathcal{S}^f + \mathcal{S}^\gamma + \mathcal{S}^c \end{bmatrix}_h d\mathbf{x} \end{aligned} \quad (49) \quad \boxed{\text{phi}}$$

Please note that the fluctuation integral is evaluated with respect to the actual parametric coordinates after using $d\mathbf{x} = \bar{J}_A d\mathcal{X}$. The predicted nodal values w_i^* are computed from

$$|\mathcal{C}_i^{n+1}|(w_i^* - w_i^n) = -\Delta t \sum_{K \ni i} \tilde{\Phi}_i^K(w_h^n, b_h^n) \quad (50) \quad \boxed{\text{RC-pred}}$$

with the $\tilde{\Phi}_i^K$ defining a splitting of the *geometrically non-conservative* fluctuation (cf. [\(Appendix D\)](#))

$$\begin{aligned} \sum_{j \in K} \tilde{\Phi}_j^K = \tilde{\Phi}^K = \oint_{\partial K} \sqrt{G} \begin{bmatrix} hu^j \\ hu^i u^j \end{bmatrix}_h n^j ds + \int_K \sqrt{G} \begin{bmatrix} 0 \\ G^{ij} (\partial_{x^j} (gh^2/2) + gh \partial_{x^j} b) \end{bmatrix}_h d\mathbf{x} \\ - \int_K \sqrt{G} \sigma^j \frac{\partial w_h}{\partial x^j} d\mathbf{x} + \int_K \sqrt{G} \begin{bmatrix} 0 \\ \mathcal{S}^f + \mathcal{S}^\gamma + \mathcal{S}^c \end{bmatrix}_h d\mathbf{x} \end{aligned} \quad (51) \quad \boxed{\text{phi-t}}$$

208 **6.2. Evaluation of the integrals**

To begin with, unless explicitly specified, in all quadrature formulas we have used analytical expressions for both the Jacobian \sqrt{G} , and the metric tensor G^{ij} . At the quadrature points, the mass flux components $(hu^i)_h$ are evaluated simply using the $P1$ expansion, while velocity components are obtained from the interpolated values of momentum $(hu^i)_h$ and depth h_h . The wet/dry region is handled as discussed in [\[9, 11\]](#). Consistently with the approximation [\(38\)](#) of [Proposition 1](#), volume integrals of the unknown are computed as

$$\int_{K_0} J_A^{n+1} \sqrt{G} w_h d\mathcal{X} = \sum_{j \in K} |\mathcal{K}_j^{n+1}| w_j = \frac{|\mathcal{K}^{n+1}|}{3} \sum_{j \in K} w_j \quad (52) \quad \text{eq:vol-int}$$

In all boundary integrals, scaled constant-by-face values of the normal mesh velocity $\sigma^j n^j$ are computed consistently with the DGCL closure [\(32\)](#) and [\(37\)](#), namely

$$(\sqrt{G} \sigma^j n^j)_f := v_f \quad (53) \quad \text{eq:sigma-n}$$

209 Concerning the non-conservative ALE term in $\tilde{\Phi}^K$, this has been evaluated as

$$\int_K \sqrt{G} \sigma^j \frac{\partial w_h}{\partial x^j} d\mathbf{x} = \oint_{\partial K} \sqrt{G} w_h \sigma^j n^j ds - \int_K w_h \frac{\partial \sqrt{G} \sigma^j}{\partial x^j} d\mathbf{x} \quad (54)$$

210 where the face values [\(53\)](#) are used in the boundary integral, while the element integral is evaluated by
211 means of the constant divergence of the DGCL [\(37\)](#):

$$\int_K \sqrt{G} \sigma^j \frac{\partial w_h}{\partial x^j} d\mathbf{x} = \sum_{i \in K} v_{f_i} w_{f_i} - w_K \frac{|\mathcal{K}^{n+1}| - |\mathcal{K}^n|}{\Delta t} = \sum_{i \in K} v_{f_i} (w_{f_i} - w_K) \quad (55)$$

where the average values w_f and w_K are simple arithmetic averages over the faces and over the element. The integrals of the source terms in [\(49\)](#) and [\(51\)](#) are computed as

$$\int_K \sqrt{G} S d\mathbf{x} \approx \frac{|\mathcal{K}|}{3} \sum_{j \in K} S_j \quad (56)$$

Finally, the hydrostatic term is computed as

$$\begin{aligned} \int_K \sqrt{G} G^{ij} (\partial_{x^j} (gh_h^2/2) + gh_h \partial_{x^j} b_h) d\mathbf{x} &= \int_K \sqrt{G} G^{ij} gh_h \overbrace{(\partial_{x^j} h_h + \partial_{x^j} b_h)}^{\partial_{x^j} \eta_h} d\mathbf{x} \\ &= \left(\int_K \sqrt{G} G^{ij} gh_h d\mathbf{x} \right) \partial_{x^j} \eta_h|_K \approx |K| \left(\sum_q \omega_q \sqrt{G} G^{ij}(\mathbf{x}_q) gh_h(\mathbf{x}_q) \right) \partial_{x^j} \eta_h|_K \end{aligned} \quad (57) \quad \text{eq:hyd}$$

212 Several (second or higher order) quadrature formulas have been tested for the term in parentheses without
213 any visible impact on the results.

214 **6.3. Distribution of the residual and main properties**

In RD schemes stability and accuracy properties depends on how the residual is distributed. The computation of the split residuals for the two RK steps Φ_i^K and $\tilde{\Phi}_i^K$ is performed following *exactly* the

steps discussed in [Ric:15]. In particular, following the construction in the reference, the residual splitting (eq:rd-split1) (46) can be more explicitly written as

$$\Phi_i^K = \beta_i^K \Phi^K + \delta(w_h) \beta_i^{\text{SD}} \Phi^K + \delta(w_h) \sum_{j \in K} m_{ij}^* \frac{w_j^* - w_j^n}{\Delta t} \quad (58) \quad \boxed{\text{eq:RD}}$$

In the above expression, the first term is the consistent one, namely the one satisfying $\sum_j \beta_j^K = 1$. The last two terms do not contribute to the consistency of the method, as indeed one can show that [Ric:15, RiA:10] [11, 46]

$$\sum_{j \in K} \beta_{j \in K}^{\text{SD}} \Phi^K + \sum_{j \in K} \sum_{k \in K} m_{jk}^* \frac{w_k^* - w_k^n}{\Delta t} = 0 \quad (59)$$

215 These additional terms are essentially stabilization terms allowing to avoid spurious modes appearing in
 216 smooth regions (cf. [Abg:06, RiB:09] for details), and can be embedded in the last integral in (46). The first one is a
 217 streamline upwind type stabilization, the second is a correction to a mass-lumping operator. These terms
 218 are in practice evaluated exactly as discussed in [Abg:06, RiB:09, Ric:15] to which we refer for details. Concerning the
 219 first term, as in [Ric:15] it is a distribution based on a blending, via the smoothness sensor $\delta(w_h)$, between
 220 a central splitting and a limited nonlinear splitting. The latter is obtained using a standard procedure
 221 in RD schemes involving the application of a bounded and sign-preserving mapping to a first order and
 222 positivity preserving Lax-Friedrich's like distribution (see for example [50] or the chapters [AR:17, Dec:17] [45, 44]). This
 223 allows to combine formal second order of accuracy with depth non-negativity preservation.
 224 Finally note that the distribution functions for the predictor step (50) are easily deduced from (58) setting
 225 $w^* = w^n$, and replacing Φ^K by $\tilde{\Phi}^K$.

226
227
228
229
230
231

Remark 2. (Metric terms treatment, accuracy, stability). *It is worth noting that the scheme is formally identical to the one obtained in the planar case. The treatment of the geometric source term boils down to the modification of the cell residual. This is a substantial simplification when conceiving and coding the scheme compared to other methods (e.g Finite Volume).*

232
233
234
235
236
237
238

Concerning the properties of the final discretization, the two main tools of analysis are a consistency property w.r.t. a variational form evaluated for smooth solutions, and a positivity preserving property rooted in the positive coefficient schemes theory (see [AR:17, Dec:17] [45, 44] and references therein). For the schemes used here, high order of accuracy is formally ensured by the boundedness of the distribution matrices, and more generally of the test functions $\{w_j\}_{j \in K}$ in (46). For the analysis of the depth positivity-preservation property of this Lax-Friedrich's-type scheme (as well as of the one obtained applying the limiter), the interested reader can refer to [Ric:15] [11] for the Eulerian case. In the ALE case, an additional limiting step is

239 required, as proposed in [1]. This is to control the mismatch between the update in the mass equation,
 240 performed in terms of η , and the one of the bathymetry based on (65) and not on the ALE remap.

241

242 6.3.1. Well-balancedness, DGCL and mass conservation

243 The first property we can easily show is the following.

244

245 **Proposition 2.** (DGCL and well-balanced on the sphere) *For any given mesh displacement on the*
 246 *sphere, the residual distribution prototype (47)-(51), with the quadrature strategy defined in Proposition 1*
 247 *and by (55) and (57), and with the distribution functions (58) verifies the C-property on moving and fixed*
 248 *meshes, as well as for Cartesian and curvilinear coordinates.*

249

250 *Proof.* The proof is obtained by applying the scheme to the initial solution $\mathbf{w}^0 = [\eta_0, 0, 0]^t$. With
 251 the hypotheses made, and by virtue of (55) combined with (51), and using (57) with η constant over the
 252 mesh, we deduce immediately that $\tilde{\Phi}^K = 0$, thus $\tilde{\Phi}_i^K = 0$, and $\mathbf{w}_i^* = \mathbf{w}_i^0$.

In the corrector step the element residual, evaluated with constant η and invoking (57), reduces to

$$\Phi^K = \frac{|\mathcal{K}|^{n+1} - |\mathcal{K}|^n}{\Delta t} \mathbf{w}^0 - \sum_{j \in K} v_{f_j} \mathbf{w}^0 = 0 \quad (60)$$

253 due to the definition of v_f . Combined with the previous results and (58) this implies $\mathbf{w}^{n+1} = \mathbf{w}^0$. \square

This proposition corroborates the choices made in the previous sections concerning the form of the SWEs. As already mentioned, however, the choice of \mathbf{w} as a main unknown has a drawback concerning mass conservation. Indeed if we sum both (47) and (50) over all the mesh nodes we obtain

$$\sum_i |\mathcal{C}_i^{n+1}| \mathbf{w}_i^{n+1} - \sum_i |\mathcal{C}_i^{n+1}| \mathbf{w}_i^* = -\Delta t \sum_i \sum_{K \ni i} \Phi_i^K = -\Delta t \sum_K \sum_{i \in K} \Phi_i^K = -\Delta t \sum_K \Phi^K \quad (61)$$

Using (48) and (52) we can further modify the mass balance to

$$\sum_i |\mathcal{C}_i^{n+1}| \mathbf{w}_i^{n+1} - \sum_i |\mathcal{C}_i^n| \mathbf{w}_i^n = -\frac{\Delta t}{2} \sum_K \Phi^K (\mathbf{w}_h^n, b_h^n) - \frac{\Delta t}{2} \sum_K \Phi^K (\mathbf{w}_h^*, b_h^{n+1}) \quad (62)$$

If we only consider the mass equation, the right hand side gives

$$-\frac{\Delta t}{2} \left[\sum_K \left(\oint_{\partial K} \sqrt{G} (hu^j - \eta \sigma^j)_h^n n^j + \oint_{\partial K} \sqrt{G} (hu^j - \eta \sigma^j)_h^* n^j \right) \right] = 0 \quad (63)$$

face integrals of neighbor elements canceling each other. As a consequence we end with

$$\sum_i |\mathcal{C}_i^{n+1}| h_i^{n+1} = \sum_i |\mathcal{C}_i^n| h_i^n - \left(\sum_i |\mathcal{C}_i^{n+1}| b_i^{n+1} - \sum_i |\mathcal{C}_i^n| b_i^n \right) \quad (64) \quad \boxed{\text{mass-error}}$$

As remarked in [\[1\]](#) the error in total mass conservation is related to the error in satisfying a discrete ALE remap of the bed. To minimize the mass error, we use here the same technique proposed in [\[1\]](#). We set:

$$|C_i^{n+1}|b_i^{n+1} := \int_{C_i^0} J_A^{n+1} \sqrt{G} \hat{b}(\boldsymbol{\chi}) d\boldsymbol{\chi} \quad (65) \quad \text{eq:batale}$$

where $\hat{b}(\boldsymbol{\chi})$ is a high resolution (analytical, or reconstructed using a finer mesh) description of the topography. We then evaluate the last integral using a higher order quadrature as done in [\[1\]](#). In particular, if the quadrature is of order κ we have, considering a smooth enough manifold:

$$\sum_i |C_i^{n+1}|b_i^{n+1} = \sum_i \int_{C_i} J_A^{n+1} \sqrt{G} \hat{b}(\boldsymbol{\chi}) d\boldsymbol{\chi} + \sum_i \mathcal{O}(h^{\kappa+3}) = \int_{M^2} \sqrt{G} b(\boldsymbol{x}) d\boldsymbol{x} + \mathcal{O}(h^{\kappa+1}) \quad (66)$$

where the $\mathcal{O}(h^{\kappa+3})$ is the local error modeled as a polynomial of degree (at least) $\kappa + 1$, readily obtained using e.g. a truncated Taylor series, and accounting for the fact that $|\mathcal{K}| = \mathcal{O}(h^2)$. The second equality uses [\(19\)](#). Note now that the first term in the final expression is actually time independent as long as $M^2 = M_0^2$, which is in practice the case. Since also the integrand is a time independent quantity, we have

$$\left| \sum_i |C_i^{n+1}|b_i^{n+1} - \sum_i |C_i^n|b_i^n \right| = \mathcal{O}(h^{\kappa+1}) \quad (67)$$

254 which combined with [\(64\)](#) shows that we can conserve h within an arbitrary accuracy.

255 7. Adaptive mesh movement strategy

sec:mmpde

The mesh adaptation technique used here is based on an error dependent mesh movement. The main principle is to define a mapping $A(\boldsymbol{\chi}, t)$ from a reference/initial configuration, described by the coordinate $\boldsymbol{\chi}$, to a physical mesh described by coordinate \boldsymbol{x} , such that the error associated to a certain density is equi-distributed. The error density is often referred to as a *monitor function* $m(\boldsymbol{x})$ [\[51\]](#). [The differential form of this principle is referred to as Moving Mesh Partial Differential Equation or MMPDE for short.](#)

The simplest method in the multidimensional case is the elliptic generator based on the MMPDE:

$$\frac{\partial}{\partial \chi^i} \left(m \frac{\partial x^\alpha}{\partial \chi^i} \right) = 0 \quad \alpha = 1, 2 \quad (68) \quad \text{eq:mmpde-ch}$$

This PDE is the Euler-Lagrange equation corresponding to the minimization of the energy functional [\[52\]](#):

$$E(\boldsymbol{x}) = \frac{1}{2} \int_{\Omega_x} m \|\nabla \boldsymbol{x}\|^2 d\boldsymbol{\chi} = \frac{1}{2} \int_{\Omega_x} m \frac{\partial x^\alpha}{\partial \chi^i} \frac{\partial x^\alpha}{\partial \chi^i} d\boldsymbol{\chi}. \quad (69) \quad \text{eq:efun-ch}$$

256 It consists in a set of decoupled quasi-linear elliptic equations mapping each coordinate. Many efficient
257 numerical methods are available to solve [\(68\)](#). The counterpart of its simplicity is that special care must

258 be taken to avoid the degeneration of the quality of the mesh, or mesh tangling. If carefully implemented,
 259 the MMPDE (68) can be quite effective (see, e.g. [TaT:03, JIN200668, ChT:08, XuN:13, Zho:13, ZhC:13, PAN2015207
 [53, 54, 55, 56, 20, 40, 57] and references therein).

The design of moving mesh methods on the sphere is a relatively recent subject of research. Optimal transport method have been discussed in [WeB:16, McR:18 [58, 59] using finite differences or finite-elements to solve the Monge-Ampere type nonlinear PDEs involved. The results shown in terms of mesh quality and mesh refinement are very interesting. It is however unclear whether the error reduction compensates the CPU time overhead of mesh adaptation. Based on our previous experience, here we have opted for a simpler version of mesh movement on the sphere, trying to remain as much as possible close to the simplicity of (68). It is known that functional (69) can be generalized to model a mapping $A : \mathcal{S}_{A_0}^2 \rightarrow \mathcal{S}_A^2$ $\mathbf{x} = A(\boldsymbol{\chi}, t)$, from a computational sphere with metric tensor G_{ij} and local coordinates $\boldsymbol{\chi}$ to a physical sphere with metric $H_{\alpha\beta}$ and local coordinates \mathbf{x} :

$$E(\mathbf{x}) = \frac{1}{2} \int_{\Omega_{\boldsymbol{\chi}}} m G^{ij} H_{\alpha\beta} \frac{\partial x^\alpha}{\partial \chi^i} \frac{\partial x^\beta}{\partial \chi^j} \sqrt{G} d\boldsymbol{\chi}. \quad (70) \quad \text{eq:hm-e}$$

Unfortunately, the above functional is similar to the harmonic map energy of [DiL:06 [60] where it is shown that the minimization problem associated may lack a unique solution. This is what has led several authors to consider more complex techniques [DiL:06, WeB:16, McR:18 [60, 58, 59]. To obtain a simpler formulation, we propose to use a mapping from the reference sphere to the parametrization of the adapted one. So we map the sphere to a plane $A : \mathcal{S}_{A_0} \rightarrow \mathbf{E}^2$ $\mathbf{x} = A(\boldsymbol{\chi}, t)$. This corresponds to a flat target metric is $H_{\alpha\beta} = \delta_{\alpha\beta}$ and to an energy functional:

$$E(\mathbf{x}) = \frac{1}{2} \int_{\Omega_{\boldsymbol{\chi}}} m G^{ij} \frac{\partial x^\alpha}{\partial \chi^i} \frac{\partial x^\alpha}{\partial \chi^j} \sqrt{G} d\boldsymbol{\chi} = \frac{1}{2} \int_{\Omega_{\boldsymbol{\chi}}} m G^{ii} \frac{\partial x^\alpha}{\partial \chi^i} \frac{\partial x^\alpha}{\partial \chi^i} \sqrt{G} d\boldsymbol{\chi} \quad (71) \quad \text{eq:hm-e2}$$

having used the fact that G^{ij} is diagonal. In practice, all goes similarly to when mapping two planes. The catch is that when minimizing (71), we will obtain an adapted mesh which will depend on the parametrization. In our opinion this is not a problem as long as the same parametrization is used for the flow equations. The MMPDE obtained in this case is

$$\frac{1}{\sqrt{G}} \frac{\partial}{\partial \chi^i} \left(m \sqrt{G} G^{ii} \frac{\partial x^\alpha}{\partial \chi^i} \right) = 0 \quad (72) \quad \text{eq:mmpde-chs}$$

260 which, as in the Cartesian case, constitutes a decoupled system of PDEs in which the only non-linearity
 261 is associated to the monitor function $m = m(\mathbf{x})$ which will depend on the solution (as in the Cartesian
 262 case). We use a straightforward P^1 Finite Element method to discretize the MMPDE, and a Newton-
 263 Jacobi iteration to update nodal displacements reading

$$\boldsymbol{\delta}_i^{k+1} = \boldsymbol{\delta}_i^k - \left(\sum_{K \ni i} a_{ii}^K \right)^{-1} \sum_{K \ni i} \sum_{j \in K} a_{ij}^K (\mathbf{x}_j^k)_K, \quad \mathbf{x}_i^{k+1} = \mathbf{x}_i^k + \boldsymbol{\delta}_i^{k+1}, \quad (73)$$

264 with a_{ij}^K the entries of the stiffness matrix arising from a straightforward finite element approximation
 265 of (72), with the only source of nonlinearity being the monitor function $m = m(\mathbf{x})$. In some of the
 266 computations a standard Laplacian mesh smoothing step is also added [HuR:97,BuH:09
 [61, 62].

267 To test the moving mesh algorithm we use a benchmark from [McR:18
 [59]. The monitor function is:

$$m = 1 + 10 \operatorname{sech}^2 \left(5 \left(\|x - x_1\|^2 - \frac{\pi^2}{4} \right) \right) + 10 \operatorname{sech}^2 \left(5 \left(\|x - x_2\|^2 - \frac{\pi^2}{4} \right) \right) \quad (74)$$

268 with $x_{1,2} = (\pm \frac{\sqrt{3}}{2}, 0, -\frac{1}{2})$. The resulting mesh is shown in figure 2. The mesh is highly compressed
 269 around the bands. The result is quite close to those presented in [McR:18
 [59], although clearly the optimal
 270 transport method of the reference gives a smoother mesh. Somewhat nicer results are obtained when
 271 including Laplacian smoothing, as shown on the right picture on the same figure.

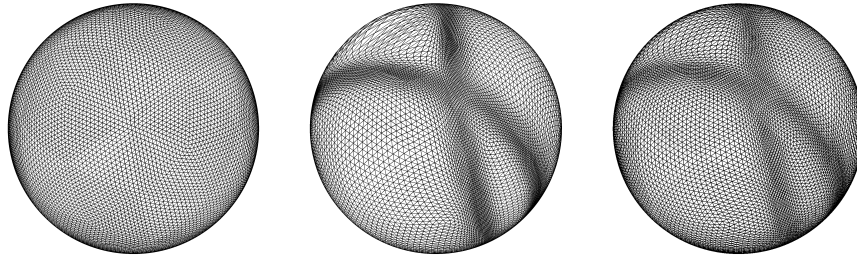


Figure 2: Adaptation to the monitor function (74). Left: computational (icosahedral) mesh. Center: adaptation without smoothing. Right: adaptation with Laplacian smoothing with smoothing coefficient 1/2.

fig:t5-t6

subsec:mon

7.1. Monitor function

In this paper we use the arc-length type monitor function of [Win:67
 [63]:

$$m = \sqrt{1 + \alpha_i f_{i*}^2}, \quad f_{i*} = \min \left(1, \frac{f_i}{\beta \max_{\mathbf{x} \in \Omega} f_i} \right) \quad (75)$$

eq:omega

273 In the tests of section 8, the physical quantities f_i have been chosen depending on the phenomenon under
 274 study. For gravity waves, we have selected, as in [ZhC:13
 [40], only one term $f_1 = \|\nabla \eta\|$ the free surface gradient,
 275 in order to detect free surface wave patterns and bore development. In presence of wet/dry transitions as
 276 in [ArR:17
 [1] we have added a second term $f_2 = F(h)$ where the function F is a regularized Heaviside function
 277 going from 1 to zero in vicinity of dry regions. When considering barotropic instability we have taken
 278 $f_1 = \|\nabla \times \mathbf{u}\|$ and $f_2 = \|\nabla \nabla \times \mathbf{u}\|$ in order to follow roll-up of the vorticity field. For all other details on
 279 our implementation of the MMPDE method please refer to [ArR:17
 [1] and references therein. The values of the
 280 tuning coefficients α_i, β are given for each test in section 8.

281 *7.2. Moving Mesh PDE-ALE algorithm*

282 For adaptive computations, the MMPDE-ALE algorithm starts with a triangulation at time n and
 283 the solution w_h^n . Setting the initial conditions for the MMPDE $m_h^1 = m_h^n$ and $\mathbf{x}^1 = \mathbf{x}^n$, where m_h^n is the
 284 monitor function evaluated with w_h^n , we proceed as follows.

285 DO k=1,kmax

286 Step 1. Move the mesh according to the Newton-Jacobi iteration (69).

287 Step 2. Use the ALE schemes to get a remap on the new mesh as discussed e.g. in [ArR:17] and re-evaluate
 288 the monitor function using the new solution

289 ENDDO

290 Step 3 Let $\mathbf{x}^{n+1} = \mathbf{x}^{kmax+1}$ define the new triangulation, evolve the underlying balance law in ALE
 291 framework on the half time step mesh as discussed in section [sec:RD]

292 Step 5. IF ($t = T_{\text{final}}$) EXIT ELSE GO TO Step 1.

293 As remarked in [ArR:17], the remap from one mesh to the new one here is only needed to evaluate the error
 294 function. This allows to simplify the mapping if necessary. The interested reader can refer to [ArR:17] for a
 295 discussion.

296 **8. Numerical experiments**

sec:exp

297 In all computations presented hereafter we have set, unless otherwise stated, $R = 6371.22 \times 10^3 m$,
 298 $g = 9.80616 m^2 s^{-1}$ and $\Omega = 7.295 \times 10^{-5} s^{-1}$. Meshes with two topologies have been tested: one generated
 299 with the unstructured mesh generator Gmsh [GuR:97], and more regular icosahedral grids. The typical mesh
 300 topologies are illustrated on figure [fig:sphere-mesh]. Adaptation is performed with 5 iteration of the Newton-Jacobi
 301 method [eq:relax]. Whenever additional smoothing steps are used, this is explicitly said.

302 *8.1. Fixed grid: zonal flows of Williamson et al.*

sec:zon

303 In this paragraph we test only the Eulerian (fixed grid) RD on some classical benchmarks taken from
 304 the test suite of [Wil:92]. Grid convergence studies have been conducted on 5 meshes generated with Gmsh
 305 and with reference sizes starting from $h_K R^{-1} = 0.16$ and halved from one mesh to the other. The meshes
 306 thus obtained are composed of 1306, 4990, 19568, 75478, and 300426 triangles respectively.

307 Relative errors are evaluated following [Wil:92] as:

$$l_2 = \frac{\|e\|_{L2}}{\|h_{ex}\|_{L2}} \quad (76)$$

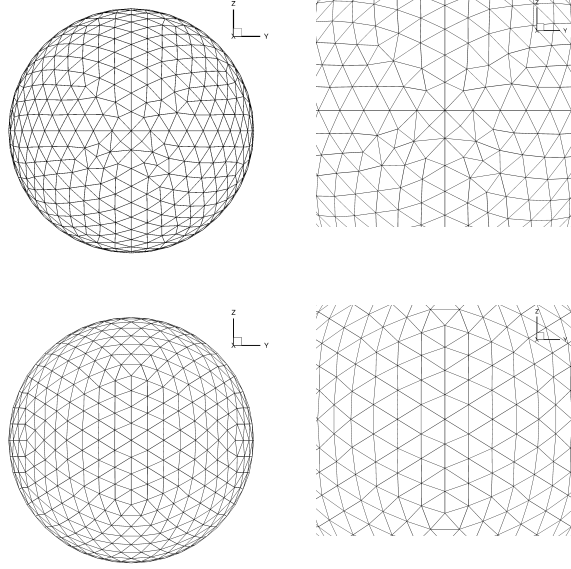


Figure 3: Computational grids on the sphere. Top row: mesh #1 generated with `gmsh`. Bottom row: third level of refinement for icosahedral mesh.

fig:sphere-mes

308 with h_{ex} the exact solution and

$$\|e\|_{L2} = \sqrt{\int_0^{2\pi} \int_{-\pi/2}^{\pi/2} (h(\mathbf{x}) - h_{ex})^2 \sqrt{G} d\mathbf{x}} \quad (77)$$

309 *Case #2* is an exact steady geostrophic equilibrium allowing to measure the order of accuracy in presence
 310 of Earth rotation. The velocity (given directly in covariant basis) and height fields are initially given by:

$$\begin{aligned} h(\mathbf{x}, 0) &= h_0 - \frac{1}{g} \left(\Omega R u_0 + \frac{u_0^2}{2} \right) (-\cos \lambda \cos \varphi \sin \alpha + \sin \lambda \cos \alpha)^2 \\ u^1(\mathbf{x}, 0) &= u_0 (\cos \alpha + \cos \varphi \tan \lambda \sin \alpha) \\ u^2(\mathbf{x}, 0) &= -u_0 \sin \varphi \sin \alpha \end{aligned} \quad (78)$$

311 with $gh_0 = 2.94 \times 10^4 m^2 s^{-2}$ and $u_0 = \frac{2\pi R}{12days}$. Two orientations are tested $\alpha = 0$ and $\alpha = \pi/4$. The errors
 312 obtained at day 5 are reported on table [2](#) below. The total error obtained on unstructured triangulations
 313 is comparable to previous results such as the Lax-Wendroff scheme on a cubed staggered grid of [\[3\]](#). The
 314 expected second order of accuracy is obtained.

315 As it is customary we report on figure [4](#) the error maps after 5 days of simulation on the fourth grid
 316 ($h_K R^{-1} = 0.02$). Particular attention should be put along the interface line (it is a discontinuity for the
 317 coordinates). Error iso-countours are very smooth for the RD scheme proposed, with seemingly no effect
 318 of the patching treatment used for the poles. For comparison we also report on figure [5](#) the error plot

grid # ($\alpha = 0$)	RD	grid # ($\alpha = \frac{\pi}{4}$)	RD
1	4.176589e-03	1	1.656259e-02
2	9.286403e-04	2	3.496469e-03
3	1.846086e-04	3	9.512542e-04
4	4.462182e-05	4	2.466671e-04
5	1.028603e-05	5	6.292595e-05
Order	2.17	Order	2.00

Table 1: Steady zonal flow. l_2 error.

tab:ch-cpu

319 relative to the computation on the fourth-level icosahedral mesh (81920 nodes) which has roughly the
 320 same reference size. The error ($\|e\|_{L_2} = 4.084761e - 05$ for $\alpha = 0$, $\|e\|_{L_2} = 2.634469e - 04$ for $\alpha = \frac{\pi}{4}$)
 321 result is very close, showing no impact of the mesh topology.

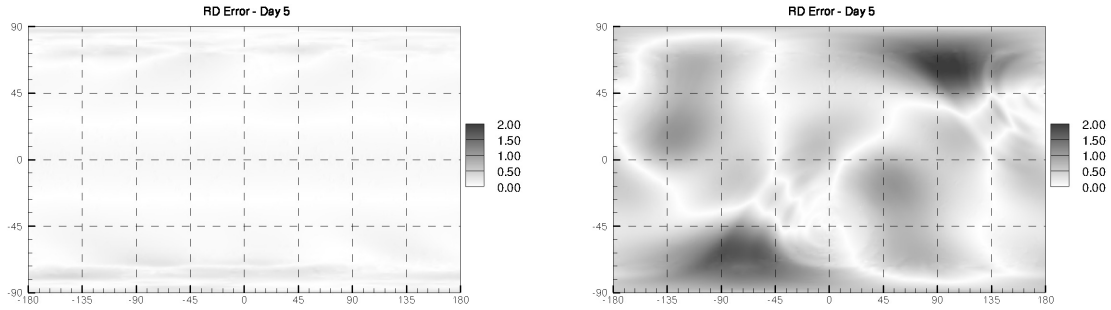


Figure 4: Steady zonal flow. Absolute value of local error on gmsh grid $h_K R^{-1} = 0.02$. Black areas correspond to $2m$ error, white areas to zero error. Left: $\alpha = 0$. Right: $\alpha = \pi/4$.

fig:zon-err

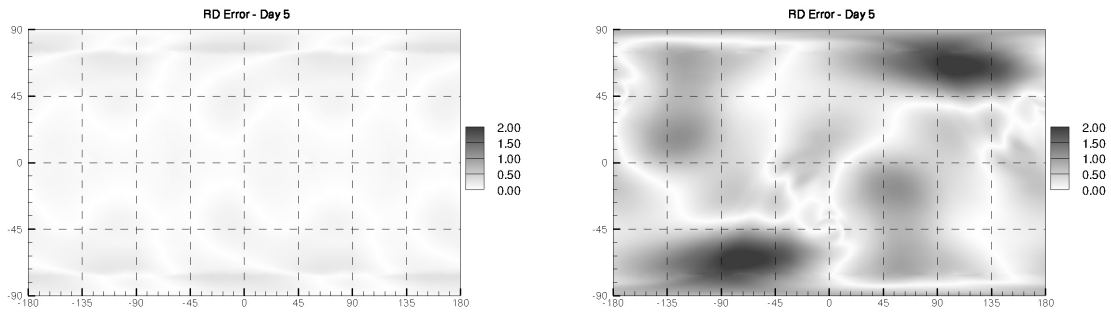


Figure 5: Steady zonal flow. Absolute value of local error on icosahedral grid (forth-level refinement) $h_K R^{-1} \approx 0.02$. Black areas correspond to $2m$ error, white areas to zero error. Left: $\alpha = 0$. Right: $\alpha = \pi/4$.

fig:zon-icoerr

Case #5 is a perturbation of the previous one. The initial velocity and height fields are given by ^{eq:wil-2}(78) with $\alpha = 0$, $h_0 = 5960 m$ and $u_0 = 20 m/s$. An isolated mountain is now added with the profile:

$$b = b_0 \left(1 - \frac{r}{R}\right) \quad (79)$$

with $b_0 = 2000 m$, $R = \pi/9$, $r^2 = \min(R^2, (\varphi - \varphi_0)^2 + (\lambda - \lambda_0)^2)$ and with the center of the cone in $(\varphi_0, \lambda_0) = (3/2\pi, \pi/6)$. Simulations are performed on the fourth mesh of the `gmsh` suite ($h_K R^{-1} = 0.02$). Figure ^{fig:mou-1}6 provides the contour lines of the water height after 5, 10, and 15 days of physical time. For this case one typically checks the conservation of total mass and energy:

$$E = h \left(\frac{1}{2} \|\mathbf{u}\|^2 + g \frac{h}{2} + gb \right), \quad (80)$$

322 Note that mass error is only related to **the change of the coordinate system across the edges that delimit**
 323 **the polar cap**. Regarding energy, none of the schemes proposed have provable energy conservation prop-
 324 erties, which makes the definition of the actual discrete evaluation of the energy somewhat arbitrary. In
 325 practice, here the energy is computed directly from nodal quantities, and then integrated using a linear
 326 approximation. The resulting error evolution is reported on figure ^{fig:mou-2}7. The evolution obtained, as well
 327 as errors obtained, for the mass and energy are comparable to or better than those typically reported
 328 in literature for computations on structured grids, and with the high resolution results by the German
 329 Weather Service (DWD) <http://icon.enes.org/swm/stswm/node5.html>.

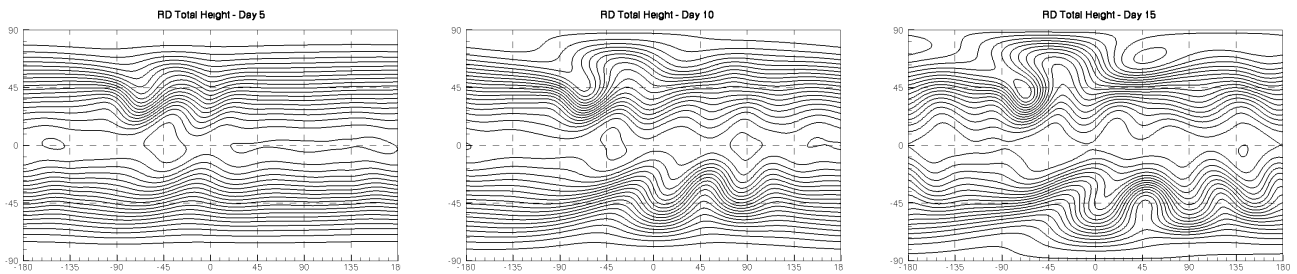


Figure 6: Zonal flow over an isolated mountain. Snapshot of the numerical solution for fixed grid simulation on `gmsh` mesh $h_K R^{-1} = 0.02$ at day 5,10 and 15. Contour levels are from 5050 m to 5950 m in intervals of 50 m.

fig:mou-1

330 8.2. Advection of cosine bell

331 To assess the numerical accuracy of our algorithm for unsteady problems and in presence of mesh
 332 movement, we revisit test #1 of the Williamson suite ^{Wil:92}[65]. For this test, the advective component is
 333 tested in isolation: only the mass equation is a prognostic equation while the wind (always expressed in

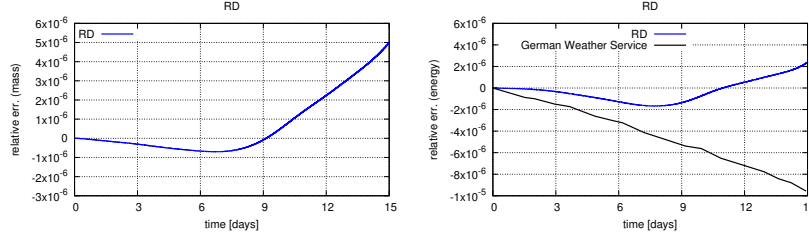


Figure 7: Zonal flow over an isolated mountain. Relative conservation error for mass (left) and energy (right) on `gms` mesh $h_K R^{-1} = 0.02$.

fig:mou-2

334 covariant components) is constant and given by

$$u^1(\mathbf{x}, 0) = u_0 (\cos \alpha + \cos \varphi \tan \lambda \sin \alpha) \quad (81)$$

$$u^2(\mathbf{x}, 0) = -u_0 \sin \varphi \sin \alpha \quad (82)$$

335 We compute the transport of a cosine bell given by:

$$h(\mathbf{x}, 0) = \begin{cases} \frac{h_0}{2} (1 + \cos(3r)) + h_0 & \text{if } r < \pi/3 \\ h_0 & \text{otherwise} \end{cases} \quad (83)$$

336 where $h_0 = 1000$, $u_0 = \frac{2\pi R}{12 \text{days}}$, and r is the great circle distance from the center of the bell (φ_C, λ_C) :

$$r = R \arccos(\sin \lambda_C \sin \lambda + \cos \lambda_C \cos \lambda \cos(\varphi - \varphi_C)) \quad (84)$$

337 We have tested two different wind directions $\alpha = 0$, and $\alpha = \pi/2$ for which the bell is transported
 338 through the north and south poles, crossing four times a polar cap interface. To test the accuracy of the
 339 ALE formulations we have added an independent unsteady motion of the mesh nodes according to the
 340 transformation:

$$\varphi(t) = \Phi + 0.5 \cos(\Phi) \cos(\Lambda) \sin\left(\frac{4\pi t}{T}\right) \quad (85)$$

$$\lambda(t) = \Lambda + 0.5 \cos(\Phi) \cos(\Lambda) \sin\left(\frac{4\pi t}{T}\right) \quad (86)$$

341 with Φ, Λ the computational or reference coordinates. The typical deformations obtained can be seen on
 342 figure [8](#). This motion will act as a background perturbation to the cosine bell advection.

343 The mesh convergence for fixed and moving meshes is reported on figure [9](#). The expected second order
 344 of accuracy is recovered. Moreover, we see roughly the same level of error for the two configurations (zonal
 345 and meridional advection). This suggests that the polar patching does not affect significantly the error
 346 constant, nor the slope. We also observe that the unsteady mesh distortion does not spoil neither the
 347 order of accuracy nor the error level. This validates the ALE formulation, at least in terms of accuracy

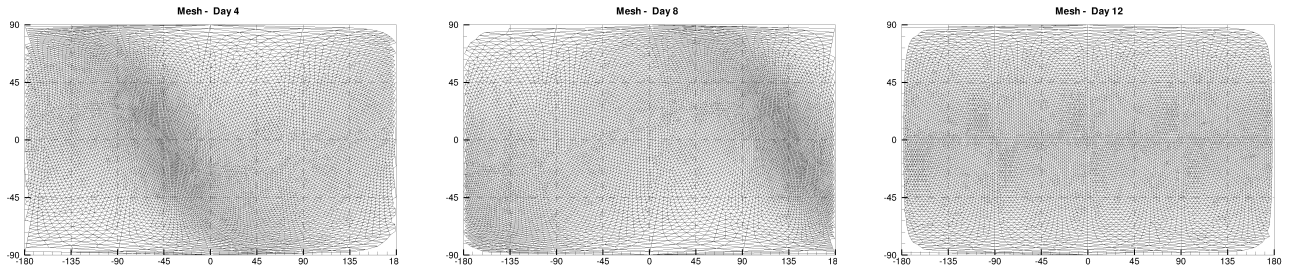


Figure 8: Advection of cosine bell. Transformed meshes number 2 at three different instants. At day 12 (final time) the transformed mesh coincides with the computational mesh.

fig:cb-mesh

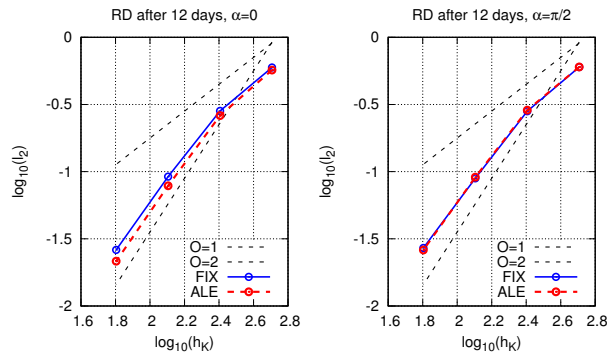


Figure 9: Advection of cosine bell: grid convergence. Left: $\alpha = 0$. Right: $\alpha = \pi/2$

fig:cb-conv

348 8.3. Circular hump

349 This is a test proposed in [Ros:04](#) [2]. The initial condition is a circular depth disturbance at the equator:

$$h(\mathbf{x}, 0) = \begin{cases} 2 & \text{if } \arccos(\cos(x^1) \cos(x^2)) \leq 0.2 \\ 0.2 & \text{otherwise} \end{cases}, \quad \mathbf{u}(\mathbf{x}, 0) = 0 \quad (87)$$

350 This initial condition is symmetric about the point $(x^1, x^2) = (0^\circ, 0^\circ)$, and should remain symmetric in
 351 absence of rotation. We run computations on two half sphere meshes generated with `gmsh`: a coarse one
 352 with 7122 points and 14034 elements; a fine one with 39699 and 78900 elements. Adaptive computations
 353 on the coarse grid are performed using the MMPDE of section [7](#) and the ALE formulation. We report
 354 the solution contours obtained with the RD scheme on figure [10](#). We can see on all meshes good shock
 355 capturing and good symmetry in all radial directions. We can observe that the mesh adaptation itself also
 356 preserves a good symmetry of the grid, and allows an extremely sharp resolution of the inner and outer
 357 shocks.

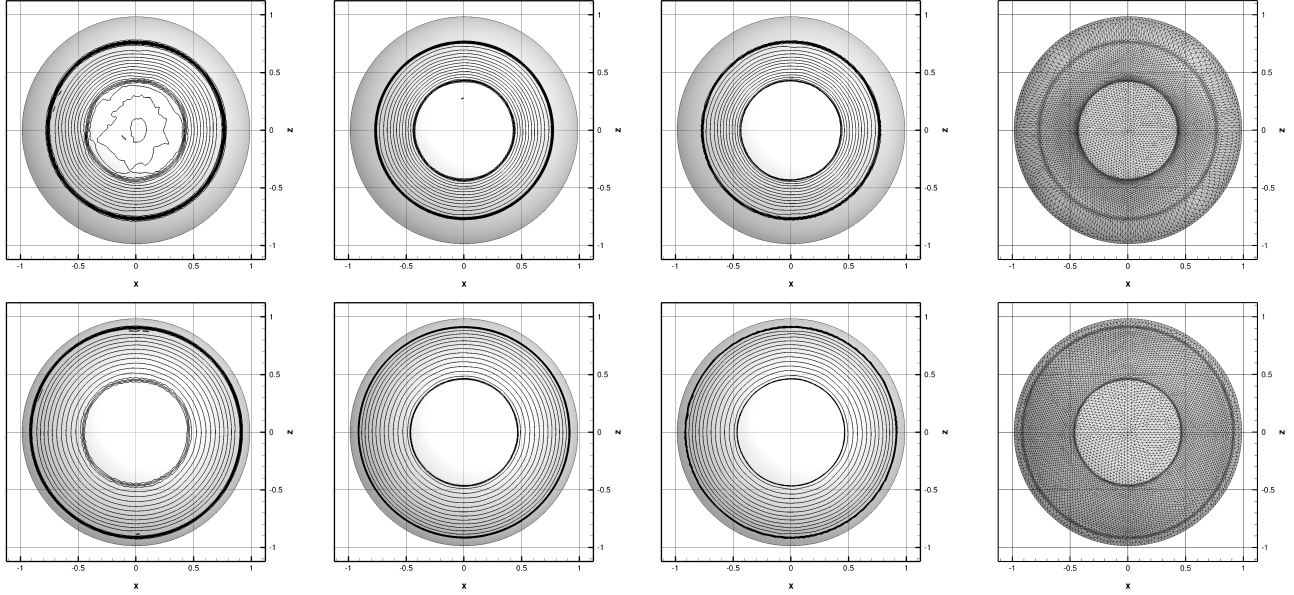


Figure 10: Circular hump on a sphere: depth iso-contours (RD solutions, 20 levels between 0 and 0.55) at times $t = 0.6$ (top) and $t = 0.9$ (bottom). From left to right: fixed coarse mesh solution, fixed fine mesh solution, ALE adaptive mesh solution, adaptive mesh.

fig:ch-iso

358 To further evaluate the results on figure [II](#) we plot the line cuts of the fluid depth along the equator.
 359 In the same figure our RD implementation is compared against the numerical solution of [\[2\]](#),^{Ros:04} obtained with
 360 high-resolution FV (Lax-Wendroff flux with MC limiter) on a Cartesian grid composed of 34680 points.
 361 We can see the sharp capturing of the discontinuities on all grids, and the improvement brought by the
 362 MMPDE adaptation on the coarse one. In these plots the adaptive mesh solution is indistinguishable
 363 from the fine mesh one.

364 Finally on table [2](#)^{tab:ch-cpu} we report the CPU times for all computations. We compute the overall time and
 365 also isolate the time associated to the MMPDE part (both mesh equation, and solution projections). We
 366 can see that the moving adaptive mesh computations are twice less expensive than the fine mesh ones,
 367 and also that even with our simplified formulation adaptation counts for non-negligible component of the
 368 simulation, more than half for the RD scheme.

369 We repeat the same test adding the effects of the rotation. We set the dimensionless rotation rate to
 370 $\Omega = 5$. In figure [II](#)^{fig:chc-iso} we report snapshots of the depth contour lines on fixed (coarse and fine) and adaptive
 371 meshes. As in the previous case, we see the higher resolution obtained with the adaptive moving mesh
 372 and the ALE formulation. This time mesh nodes are clustered both around the shock waves and also in
 373 correspondence of smoother features where high gradients appear. On table [3](#)^{tab:chc-cpu} we report the CPU times.

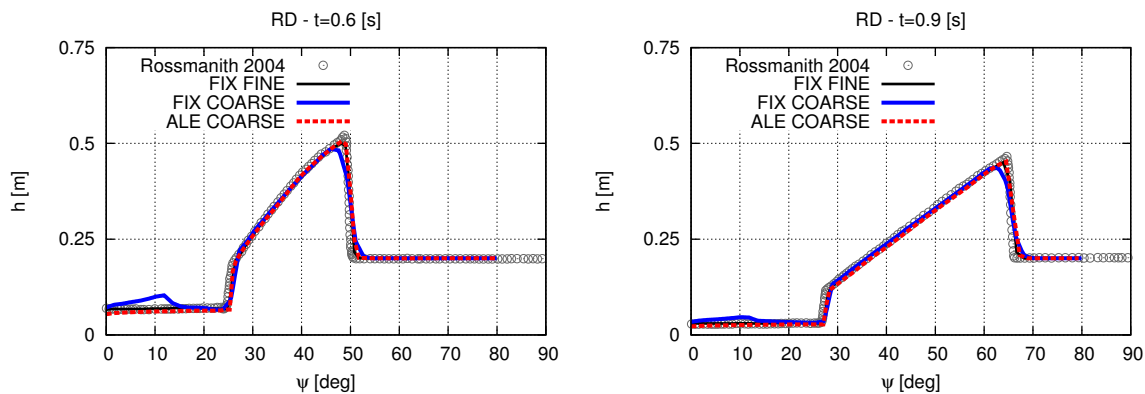


Figure 11: Circular hump on a sphere. Solution along the equator.

fig:ch-cut

ALG	Mesh (Nodes)	RD[s] (%MMPDE)
FIX-COARSE	7122	46.89
FIX-FINE	39699	674.66
ADAPT-ALE	7122	368.57 (51.5%)

Table 2: Circular hump on a non rotating sphere. CPU times.

tab:ch-cpu

374 8.4. Barotropic instability

375 This test, contained in [Gal:04](#) [66], consists of a geostrophically balanced mid-latitude jet, to which a small
 376 perturbation is added to initiate an instability. Here we test the RD scheme on a fine mesh with reference
 377 size of $h_K R^{-1} = 0.01$, and compare with adaptive simulations on coarse grids with $h_K R^{-1} \approx 0.02$.
 378 The fine mesh has roughly 300k triangles, while the coarse ones have approximately 80k triangles. For
 379 the adaptive simulations we compare results on the icosphere as well as on a `gms` mesh. In particular,
 380 adaptation has been performed using in the monitor function relative vorticity and its gradient through the
 381 formula of section [subsec:mon](#) 7.1 with $\alpha_1 = 10, \alpha_2 = 40, \beta = 0.1$. One iteration of Laplacian smoothing (smoothing
 382 coefficient 0.25) is used.

ALG	Mesh (Nodes)	RD[s] (%MMPDE)
FIX-COARSE	7122	81.39
FIX-FINE	39699	1056.39
ADAPT-ALE	7122	638.22 (50.2%)

Table 3: Circular hump on a rotating sphere. CPU times.

tab:chc-cpu

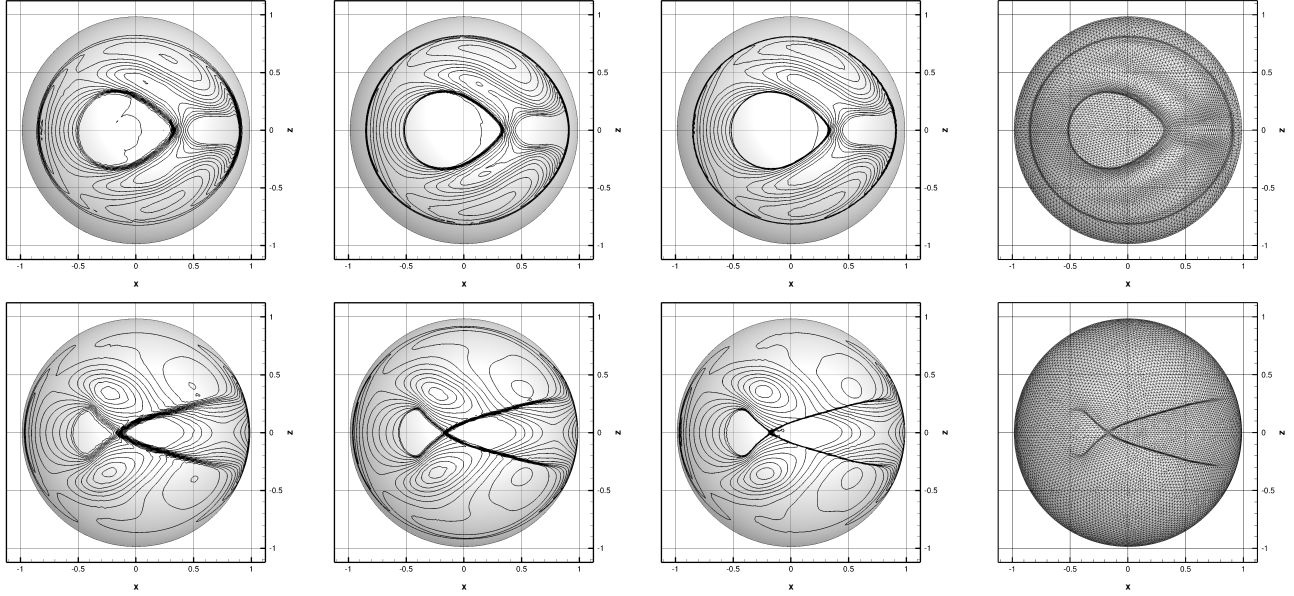


Figure 12: Circular hump on a rotating sphere: depth iso-contours (RD solutions, 20 levels between 0 and 0.55) at times $t = 0.8$ (top) and $t = 1.2$ (bottom). From left to right: fixed coarse mesh solution, fixed fine mesh solution, ALE adaptive mesh solution, adaptive mesh.

fig:chc-iso

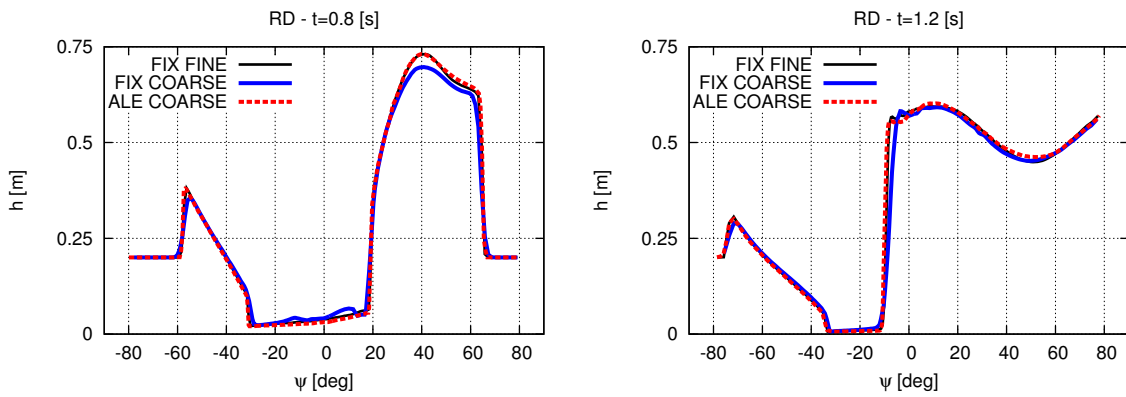


Figure 13: Circular hump on a rotating sphere. Solution along the equator.

fig:chc-cut

ALG	Mesh (Nodes)	RD [s] (%MMPDE)
FIX-FINE	<code>gms</code> h 150215	246629.4
ADAPT-ALE	<code>gms</code> h 41681	116126 (53.3%)
ADAPT-ALE	icosahedral 40962	86642.7 (52.8%)

Table 4: Barotropic instability. CPU times.

tab:jet-cpu

383 In figure [fig:gal](#) [\[4\]](#) we show the vorticity field corresponding to a physical time of 6 days. The top figure
384 reports the field obtained with the fine mesh, which is very similar to the results typically reported in
385 literature (e.g. see the high-order FV of [\[4\]](#) [\[10\]](#) and it is considered here as a reference solution. The last
386 row on the bottom show the same fixed mesh computation on the coarse grid. We can clearly see that
387 the onset of the instability as well as its evolution are wrongly reproduced on this mesh level. Note that
388 the result is the same independently on the mesh topology, the icosahedral mesh providing very similar
389 results to the one generated with `gms`h.

390 Second and third rows report the adaptive simulations on the coarse meshes. We can clearly see that
391 the adaptive mesh movement allows to correctly reproduce the global instability process, with a slight
392 smoothing of last part of the instability ($\varphi \leq \sim -180^\circ$) for the `gms`h mesh, while the result on the coarse
393 adaptive icosahedral is almost identical to the fine mesh one. 3D visualization of the vorticity fields on
394 the adaptive meshes and the corresponding meshes obtained are reported on figure [fig:gal1](#) [\[5\]](#), showing a nice
395 capturing of the instability. Finally, we report the computational times on table [tab:jet-cpu](#) [\[4\]](#): adaptive computations
396 cost more then one third of the fine mesh simulation. This is an encouraging result confirming the potential
397 of the schemes and of the mesh adaptation technique proposed here.

sec:toho

398 8.5. Adaptive simulation of the Tohoku 2011 tsunami

399 As a last application we consider the simulation of the 2011 Tohoku-Honsu tsunami with the RD scheme
400 and the MMPDE-ALE approach proposed. The computational domain is a relatively large chunk of the
401 Pacific ocean ($650 [km] \times 650 [km]$), on which an initial waveform computed in [\[67\]](#) [\[17\]](#) with the approach
402 of [\[68\]](#) [\[13\]](#) is imposed. To asses the potential of the MMPDE-ALE approach on a multiscale problem, we
403 consider the initial propagation from the source to the coast, and the runup and flooding of the complex
404 bathymetry of the coast. Both topographic data and initial wave elevation and currents are provided
405 by BRGM within the research program TANDEM (see <http://www-tandem.cea.fr>). A sketch of the
406 domain and of the initial solution is reported on figure [fig:toho0](#) [\[6\]](#). Friction is based on a constant Manning
407 coefficient of $n = 0.03125 [sm^{-1/3}]$ [\[69\]](#) [\[10\]](#).

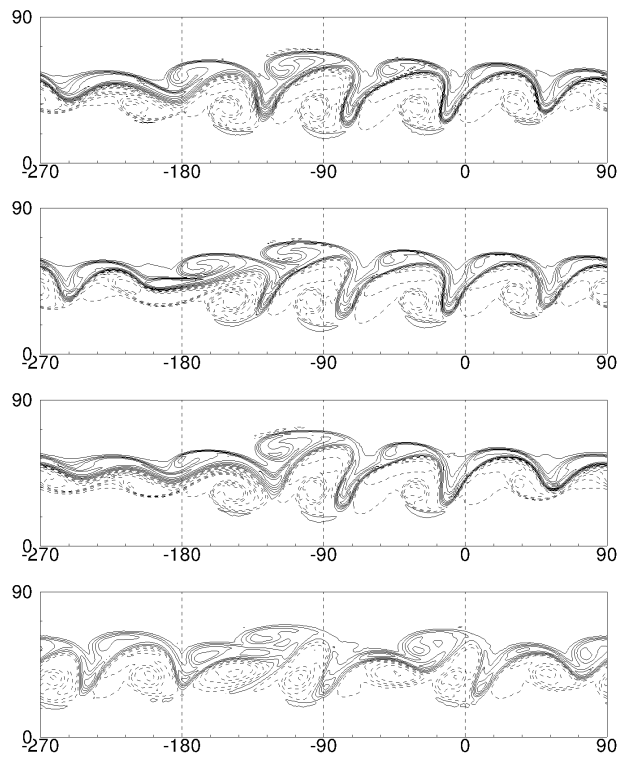


Figure 14: Barotropic instability. Vorticity field at day 6. Contour lines are from $-1.1e-4 s^{-1}$ to $-1.5e-4 s^{-1}$ in intervals of $2e-5 s^{-1}$. Top: fixed fine mesh. Second and third rows: adaptive (respectively icosahedral and `gmsh`) coarse mesh. Bottom: fixed coarse.

fig:gal

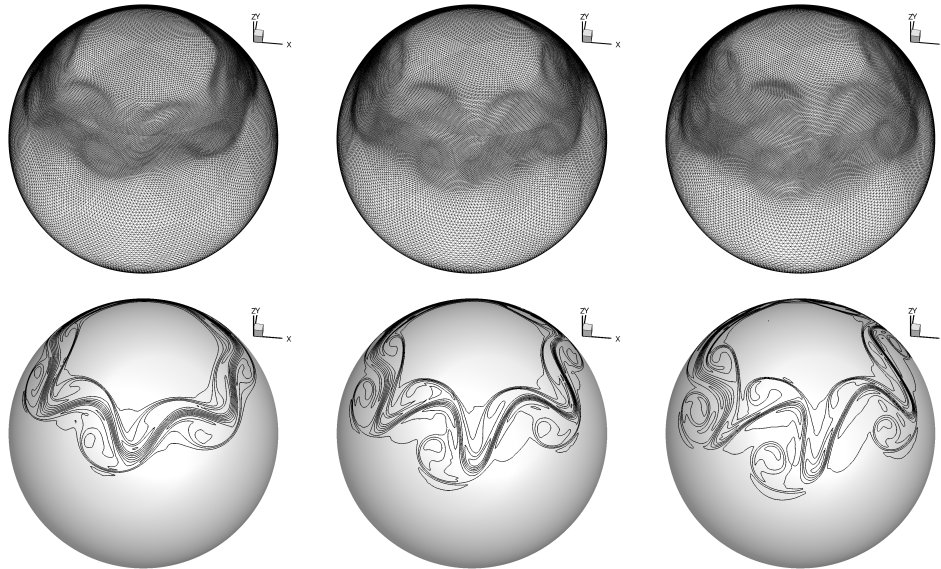


Figure 15: Barotropic instability. Relative vorticity field with corresponding adapted mesh at day 5, 5.5 and 6.

fig:gali

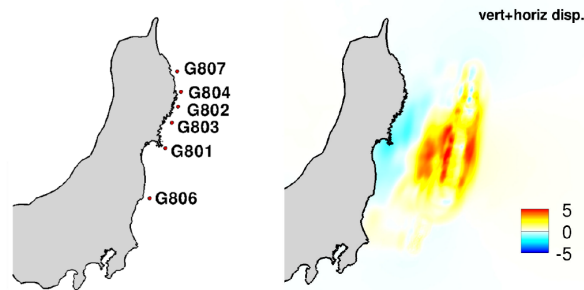


Figure 16: Tohoku-Honsu tsunami: domain with position of the GPS probes (left) and initial wave height (right). Colour legend in meters.

fig:toho0

408 A reference computation has been run on a fine unstructured mesh strongly refined in proximity of
 409 the coast, where the mesh size is reduced from 5 km used offshore to 120 [m] . The coarse mesh used for
 410 the MMPDE-ALE method has local mesh size respectively of 360 [m] in the proximity of the coast, and
 411 an offshore size of 15 km . This allows to cut by a half the number of mesh elements resulting in a mesh
 412 composed by 364864 nodes and 728874 elements. Mesh adaptation is performed as discussed in section
 413 subsec:mon 7.1 with tuning parameters $\alpha_1 = 20$, $\alpha_2 = 60$ and $\beta = 0.1$.

414 fig:fig:101-2 fig:m1-30 Figures 17, 18, and 19 provide visualizations of the first 10, 20, and 30 minutes of propagation, showing
 415 water height and the adaptive meshes obtained in vicinity of the Japanese coast. We can see how the

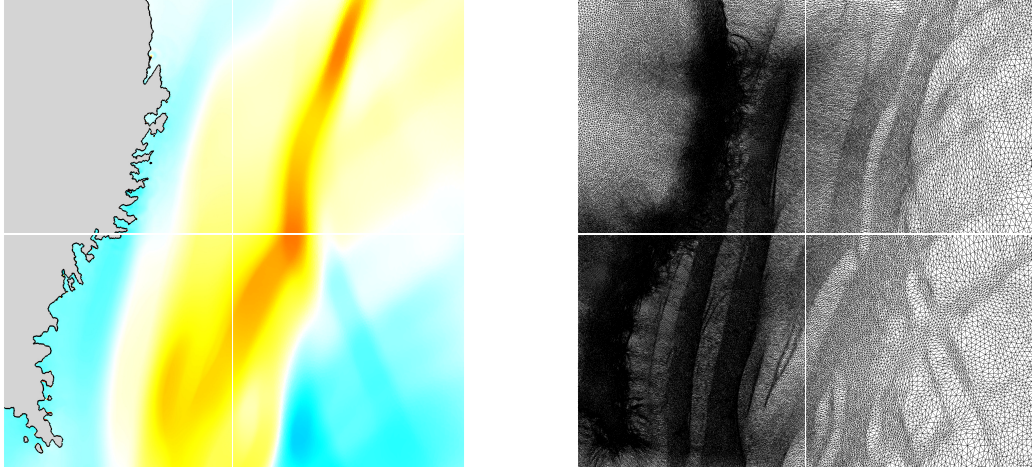


Figure 17: Tohoku tsunami. Snapshot of the free surface level (close up of the Iwate and north of the Miyagi prefectures, same colour legend of previous figures) at $t = 0:10'$ (time origin is 11 March 2011 14:51:18 LT).

fig:m1-10

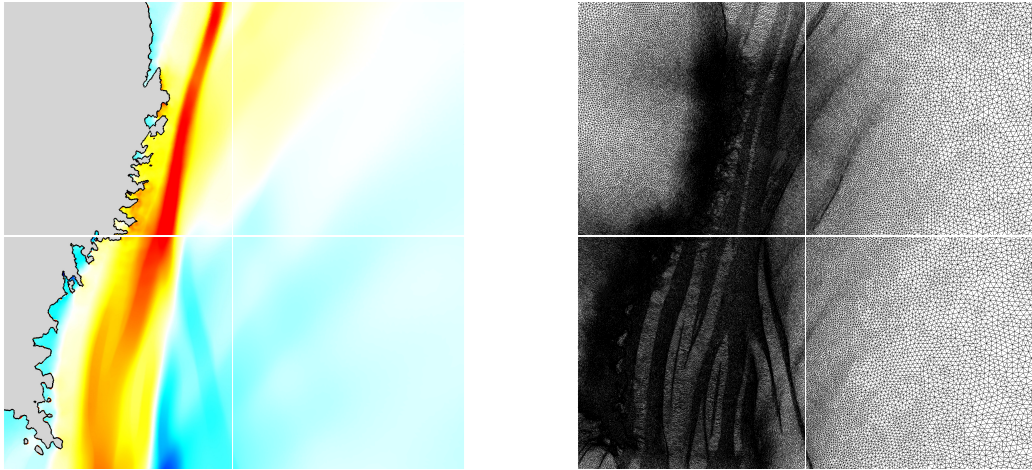


Figure 18: Tohoku tsunami. Snapshot of moving mesh (close up of the Iwate and north of the Miyagi prefectures, same colour legend of previous figures) at $t = 0:20'$ (time origin is 11 March 2011 14:51:18 LT).

fig:m1-20

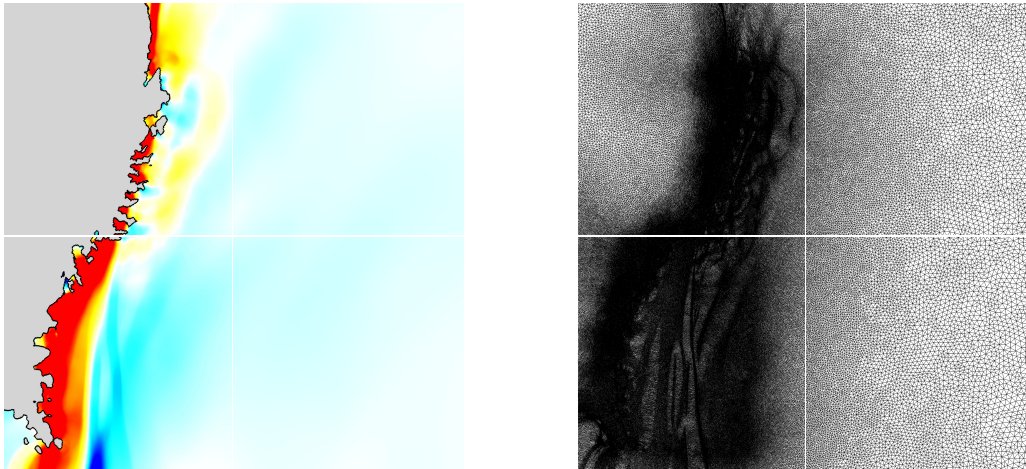


Figure 19: Tohoku tsunami. Snapshot of the free surface level (close up of the Iwate and north of the Miyagi prefectures, same colour legend of previous figures) at $t = 0:30'$ (time origin is 11 March 2011 14:51:18 LT).

fig:m1-30

416 mesh adapts to the complex tsunami wave pattern. This becomes visible especially when the wave shoals
 417 and the mesh points gather in correspondence of the largest gradients of the incoming waves train. To
 418 further evaluate the quality of the adaptive computations we compare on figure [20](#) [fig:ssh](#) the time series of the
 419 water elevation in the GPS gauges. Both the fine mesh and the adaptive ones agree quite well with the
 420 GPS observations, with an accurate computation of the arrival time and of the peak of the leading wave.
 421 The complex interaction between incoming and trapped waves that follows is also well reproduced, see
 422 others published results [\[Che:14,LoK:12,ShS:12\]](#) [\[70, 71, 72\]](#). We remark that the adaptive computations allow to reproduce the
 423 fine mesh results with half of the mesh elements.

424 We now consider the approximation of the flooding of the Japan coastal prefectures. We focus on three
 425 bays in the south of the Iwate prefecture: they are the Kesenuma, Hirota and Ofunato bay, as they appear
 426 in figure [21](#) [fig:floo-1](#), from south to north. The figure shows on the left the fine mesh with the initial coastline
 427 superimposed, a visualization of the initial coastline in the middle and the position of the inundation front
 428 after 40 minutes from the beginning of the event. The figures give an idea of the geometrical complexity
 429 of the front line, with inundation scales of the order of magnitude of 10 meters, which can be compared
 430 with the propagation scales of several hundreds of kilometers.

431 The handling of this complexity with the MMPDE is represented on figure [22](#) [fig:floo-2](#) showing the meshes
 432 adapted to the initial coastline and to the coastline after 40 minutes. We can see here the limitations
 433 of the moving mesh approach which is stretched here to its maximum. For some of the features, as for
 434 example the thinner lands close to the Osimaseto Strait and those around Hirota bay, clearly the density

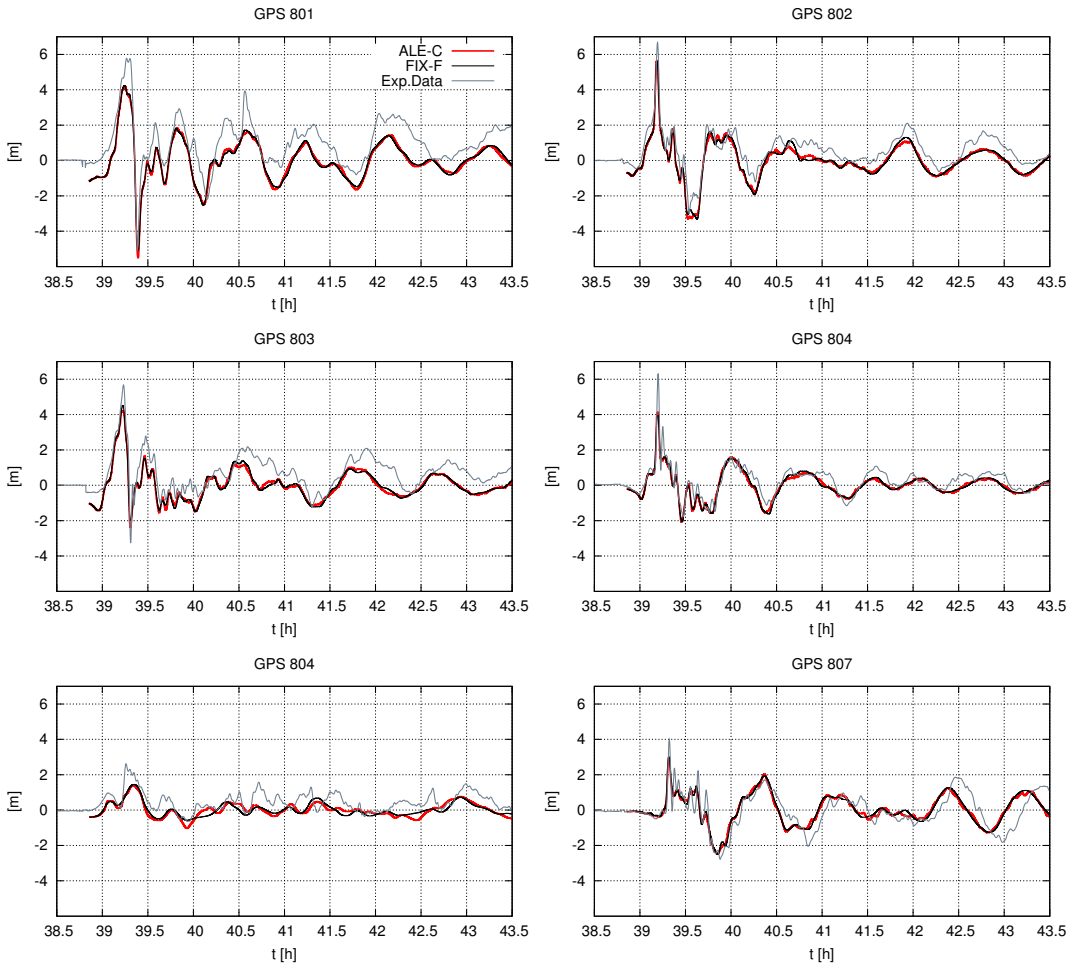


Figure 20: Simulated sea level displacement recorded at GPS buoys with fixed embedded mesh and moving embedded mesh.

fig:ssh

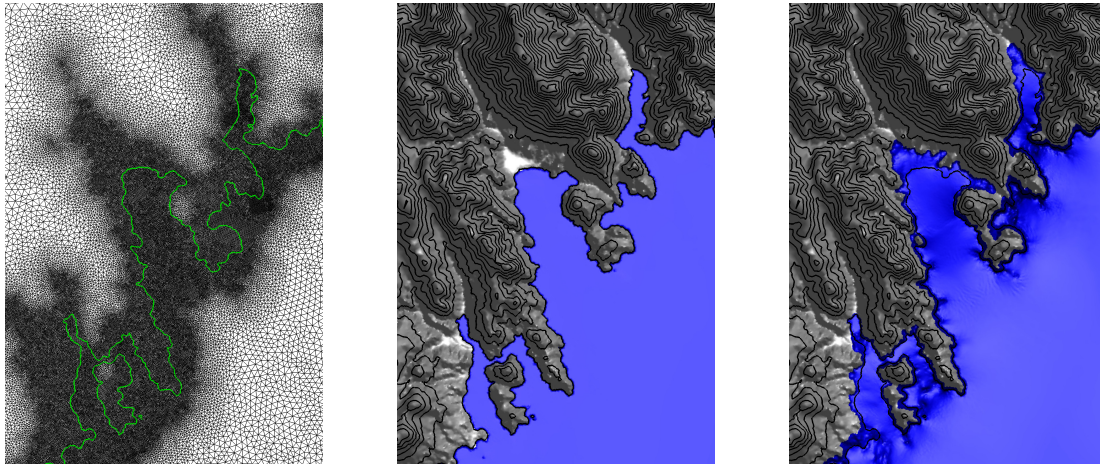


Figure 21: Tohoku tsunami. Flooding of the Iwate prefecture computed with RD scheme on fine fixed grid mesh. Left: zoom of the mesh, Right: snapshot of the inundated areas at $t = 0:00'$ and $t = 0:40'$ (time origin is 11 March 2011 14:51:18 LT).

fig:floo-1

435 of mesh nodes is not enough to allow a capturing of all the interfaces present. This results in parts of
 436 the emerged coast to be represented essentially with one stretched element. This is especially true for the
 437 mesh at 40 minutes (right picture), and has of course an impact on the approximation of the moving wet
 438 dry front in these areas. From the same picture we can also already see that the mesh follows well the
 439 inundation front obtained on the fine mesh, and visible on the rightmost picture on figure [fig:floo-1](#)
[21](#).

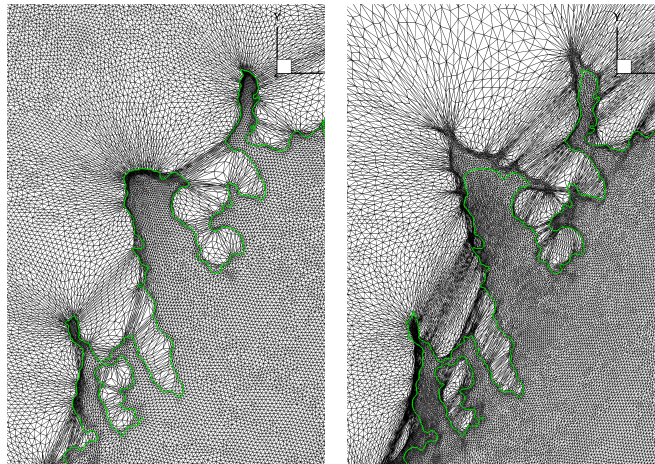


Figure 22: Tohoku tsunami. Flooding of the Iwate prefecture computed with RD scheme. Snapshot of the mesh at $t = 0:00'$ and $t = 0:40'$ (time origin is 11 March 2011 14:51:18 LT).

fig:floo-2

440 To go further in the comparison, we consider the runup plot in the same area. On figure [fig:floo-3](#)
[23](#) we report

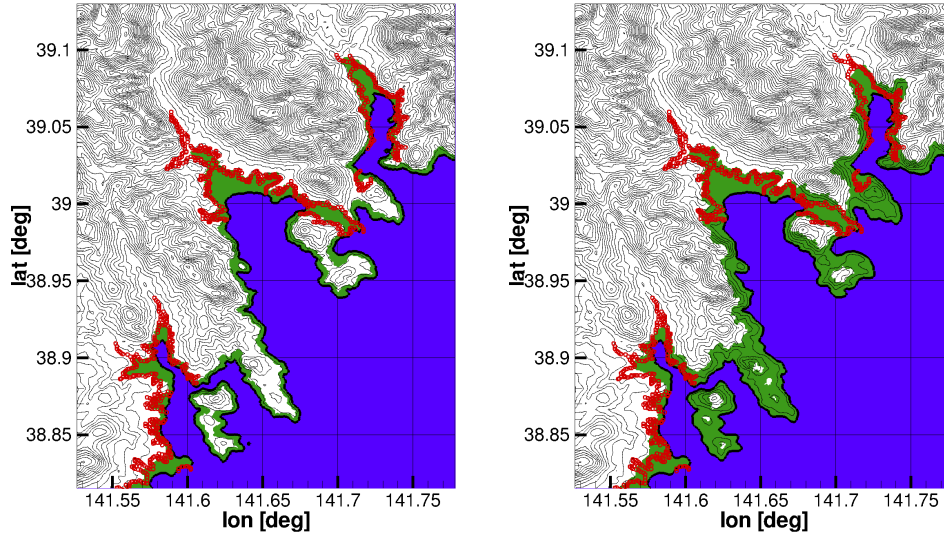


Figure 23: Tohoku tsunami. Green zones are flooded areas in Iwate prefecture. Left: fix coarse simulation. Middle: fix fine simulation. Right: adaptive ALE simulation on coarse mesh. Red dots denotes surveyed points, from [Che:14 \[70\]](#).

fig:floo-3

441 the runup obtained on the fine mesh (left picture), and with the adaptive computation (right picture).
 442 In both pictures the flooded computational areas are represented in green, while red symbols denote the
 443 surveyed inundation in the real event. The fixed fine mesh computation gives a good prediction of the
 444 runup process, with exception of some fine detail as the inundation of two narrow channels at the end of
 445 Hirota bay, which remain dry throughout the simulation.

446 The result of the MMPDE-ALE scheme is acceptable as it does cover most of the surveyed inundation
 447 areas. However, there is no improvement w.r.t. the fine mesh, and we clearly see the main limitation of
 448 the approach: the effect of the mesh stretching introduced in the dry region close to the wet/dry areas
 449 (cf. right picture on figure [fig:floo-2 \[22\]](#)) is that as soon as a point becomes wet, the inundated region covered
 450 geographically is unrealistically large. To cope with this phenomenon one could either look for a recipe to
 451 a-priori tune the density of mesh nodes, so that all features may be resolved. One may also try to move
 452 more points in the dry region to improve the resolution, however for such multi scale problems, a more
 453 realistic path is to combine the MMPDE with a re-meshing step. We think the result obtained here is a
 454 good example of the how much MMPDE can be stretched for this type of problems.

455 **9. Conclusions and outlook**

456 We have discussed approximations of the rotating shallow water equations on the sphere using fixed
457 and moving meshes. The main principles of the ALE form of the equations have been derived, and the
458 relations between the GCL and well balancedness have been shown. A numerical approximation based
459 on residual distribution has been proposed, with a numerical closure allowing to combine DGCL and C-
460 property. A simplified elliptic PDE for mesh adaptation has been proposed and tested as a basis for a time
461 dependent MMPDE-ALE method. The numerical results have shown that on fixed unstructured meshes
462 the RD scheme proposed achieves accuracy close to te one usually presented in literature on structured
463 grids. For flows with discontinuities and unstable fronts the MMPDE-ALE adaptation allows to enhance
464 this accuracy, allowing in principle a considerable reduction in CPU time. For the cases considered here
465 this reduction goes from 30% to 50%. We have also shown that for genuinely multi-scale problems, as the
466 Tohoku-Honsu tsunami computation of section ^{sec:toho}8.5, this technique reaches its limitations and a re-meshing
467 phase is clearly necessary.

468 This work is a first step toward several generalizations which will involve both higher order approx-
469 imations based on stabilized continuous polynomial approximations, an ad hoc combination of mesh
470 movement and local remeshing, and possibly improved treatments of the pole problem, following e.g. the
471 finite element mixed 3D/2D approximation proposed in ^{Bern:09}[7].

472 **Acknowledgments**

473 Work partially funded by the TANDEM contract, reference ANR-11-RSNR-0023-01 of the French
474 Programme Investissements d’Avenir. Some of the computations presented in this paper were carried
475 out using the PlaFRIM experimental testbed, supported by Inria, CNRS (LABRI and IMB), Université
476 de Bordeaux, Bordeaux INP and Conseil Régional d’Aquitaine. We are grateful to our colleagues from
477 BRGM Orléans (and in particular R. Pedreros) for useful discussions and for the data used in the Tohoku
478 simulations.

479 **Appendix A. Notation and concepts from differential geometry**

app:a1

480 This appendix recalls some basic concepts from differential geometry, and used in the main body of
481 the paper. We adopt a spacetime formalism which is better suited to time-deforming frame of reference.
482 In particular, we work with spacetime coordinates $\{x^0, x^1, x^2\}$, where the first is understood to be time

483 $x^0 = t$, while $\{x^j\}_{j=1,2}$ are purely spatial ones. In all the formulas that will follow, standard summation
 484 convention is implied, unless otherwise stated.

app:a1.184

Appendix A.1. Spherical transformation

486 We consider a steady transformation from the set of Cartesian coordinates $\mathbf{r} = \{r^1, r^2, r^3\}$ to a set of
 487 curvilinear coordinates $\mathbf{x} = \{x^1, x^2\}$. The curvilinear coordinates describe a sphere embedded in \mathbb{R}^3 with
 488 covariant vector basis which are tangent to the sphere $\{\mathbf{g}_1, \mathbf{g}_2\}$. The transformation reads:

$$\mathbf{r} = F(\mathbf{x}) \quad (\text{A.1})$$

We can define the Jacobian matrix of this mapping, and of the inverse mapping, as

$$\mathbf{J}_F = \left[\frac{\partial r^i}{\partial x^j} \right], \quad \mathbf{J}_F^{-1} = \left[\frac{\partial x^i}{\partial r^j} \right] \quad (\text{A.2})$$

An important role is played by the metric tensor \mathbf{G} , which is a symmetric tensor that allows to define a
 measure of length on the sphere $ds = G_{ij} dx^i dx^j$, with

$$G_{ij} = \mathbf{g}_i \cdot \mathbf{g}_j \quad (\text{A.3})$$

eq:Gij_def

The metric tensor can also be evaluated directly from the mapping Jacobian using the relation

$$\mathbf{G} = \mathbf{J}_F^T \mathbf{J}_F \quad (\text{A.4})$$

eq:G_J_relatio

489 The determinant of \mathbf{G} will be denoted by $G = \det \mathbf{G}$. The determinant of the transformation then reads
 490 $J_F = \sqrt{G}$. We use the inverse metric tensor \mathbf{G}^{-1} whose entries are denoted by G^{ij} . We also introduce for
 491 later use the second-kind Christoffel symbols:

$$\Gamma_{jk}^i = \mathbf{g}^i \cdot \frac{\partial \mathbf{g}_j}{\partial x^k} \quad (\text{A.5})$$

with \mathbf{g}^i the contravariant vector basis. We recall two important properties of the Christoffel symbols:

$$\frac{\partial G^{ij}}{\partial x^j} + G^{ij} \Gamma_{mj}^m + \Gamma_{jm}^i G^{mj} = 0 \quad (\text{Ricci's Lemma}), \quad \text{and} \quad \sqrt{G} \Gamma_{ij}^i = \frac{\partial \sqrt{G}}{\partial x^j} \quad (\text{A.6})$$

eq:Ric

492 for the demonstration, see [Ngu:14](#)
[\[41\]](#).

Even though the above relations are valid on general 2D manifolds, all the numerical results in this paper
 are obtained for a latitude longitude (lat-lon or λ - φ) parametrization of the sphere for which the metric
 tensor and Christoffel symbols of second kind write respectively as:

$$\mathbf{G} = \begin{bmatrix} R^2 \cos^2 \lambda & 0 \\ 0 & R^2 \end{bmatrix}, \quad \mathbf{\Gamma}^1 = \mathbf{g}^1 \cdot \frac{\partial \mathbf{g}_i}{\partial z^j} = \begin{bmatrix} 0 & -\tan \lambda \\ -\tan \lambda & 0 \end{bmatrix}, \quad \mathbf{\Gamma}^2 = \mathbf{g}^2 \cdot \frac{\partial \mathbf{g}_i}{\partial z^j} = \begin{bmatrix} \sin \lambda \cos \lambda & 0 \\ 0 & 0 \end{bmatrix} \quad (\text{A.7})$$

493 with R the sphere radius.

Appendix A.2. ALE transformation

495 In section [B](#) [sec:a1e](#) we have considered an ALE transformation in the parametric domain from the actual
 496 curvilinear coordinates $\mathbf{x} = \{x^1, x^2\}$ with covariant basis $\{\mathbf{g}_1, \mathbf{g}_2\}$ to a set of reference/ALE curvilinear
 497 coordinates $\boldsymbol{\chi} = \{\chi^1, \chi^2\}$ with covariant basis $\{\boldsymbol{\gamma}_1, \boldsymbol{\gamma}_2\}$:

$$\mathbf{x} = A(\boldsymbol{\chi}, t) \quad (\text{A.8})$$

Two different time derivatives have been introduced: the Eulerian time derivative $\frac{\partial}{\partial t}$ and the ALE one $\frac{\partial}{\partial t}\Big|_{\boldsymbol{\chi}}$. Then, the spacetime Jacobian matrix and its inverse for the ALE transformation are

$$\mathbf{J}_A = \begin{bmatrix} 1 & \frac{\partial t}{\partial \chi^j} \\ \frac{\partial x^i}{\partial t}\Big|_{\boldsymbol{\chi}} & \frac{\partial x^i}{\partial \chi^j} \end{bmatrix} = \begin{bmatrix} 1 & 0 \\ \sigma^i & \frac{\partial x^i}{\partial \chi^j} \end{bmatrix}, \quad \mathbf{J}_A^{-1} = \begin{bmatrix} 1 & \frac{\partial t}{\partial x^j} \\ \frac{\partial \chi^i}{\partial t} & \frac{\partial \chi^i}{\partial x^j} \end{bmatrix} = \begin{bmatrix} 1 & 0 \\ -\Sigma^i & \frac{\partial \chi^i}{\partial x^j} \end{bmatrix} \quad (\text{A.9})$$

eq:a1e_jac

498 In the above expression we have used the definitions of covariant mesh velocity, in actual covariant components σ^i and in reference ones Σ^i . The relationships between the two is given by $\Sigma^i = \frac{\partial \chi^i}{\partial x^j} \sigma^j$. One
 499 can show that the determinant of the ALE Jacobian reduces to the determinant of the spatial Jacobian
 500 $J_A = \det\left(\frac{\partial \chi^i}{\partial x^j}\right)$.
 501

502 For the time-dependent ALE transformation, Christoffel symbols change with time. We can express
 503 them with respect to the actual components such as in [\(A.5\)](#) or [with respect to the reference/ALE](#)
 504 [components](#):

$$\bar{\Gamma}_{jk}^i = \mathbf{g}^i \cdot \frac{\partial \mathbf{g}_j(A(\boldsymbol{\chi}, t))}{\partial \chi^k} \quad (\text{A.10})$$

505 the relationship between the two being

$$\Gamma_{jm}^i = \mathbf{g}^i \cdot \frac{\partial \mathbf{g}_j}{\partial x^m} = \mathbf{g}^i \cdot \frac{\partial \mathbf{g}_j(A(\boldsymbol{\chi}, t))}{\partial \chi^k} \frac{\partial \chi^k}{\partial x^m} \quad (\text{A.11})$$

$$= \bar{\Gamma}_{jk}^i \frac{\partial \chi^k}{\partial x^m} \quad (\text{A.12})$$

Moreover Christoffel symbols relative to the time derivative (denoted by the index 0) can be expressed by chain rule

$$\bar{\Gamma}_{j0}^i = \mathbf{g}^i \cdot \frac{\partial \mathbf{g}_j(A(\boldsymbol{\chi}, t))}{\partial t}\Big|_{\boldsymbol{\chi}} = \mathbf{g}^i \cdot \frac{\partial \mathbf{g}_j}{\partial x^m} \frac{\partial x^m}{\partial t}\Big|_{\boldsymbol{\chi}} = \Gamma_{jm}^i \sigma^m = \bar{\Gamma}_{jk}^i \frac{\partial \chi^k}{\partial x^m} \sigma^m = \bar{\Gamma}_{jk}^i \Sigma^k \quad (\text{A.13})$$

506 Finally we distinguish tensor quantities in actual covariant components $\mathbf{T} = T^{ij} \mathbf{g}_i \mathbf{g}_j$ from tensor quantities
 507 in reference covariant components $\mathbf{T} = \bar{T}^{ij} \boldsymbol{\gamma}_i \boldsymbol{\gamma}_j$.

Appendix B. ALE-SWEs on a 2D manifold derived with a spacetime approach

With the definitions of (Appendix A), the derivation of the ALE-SWEs in curvilinear coordinates is immediate. We consider only momentum conservation since the mass equation is a particular case. Momentum conservation is expressed in terms of the 4-divergence of a second order tensor \mathbf{T} . We denote, as it is custom, the first row of the tensor as the momentum vector which represents the conserved quantity, e.g. $T^{i0} = hu^i$. Then the divergence in curvilinear reference/ALE coordinates writes

$$\nabla \cdot \mathbf{T} = \frac{1}{J} \frac{\partial}{\partial t} \Big|_{\chi} \left(J \bar{h} u^i \right) + \frac{1}{J} \frac{\partial}{\partial \chi^j} \left(J \bar{T}^{ij} \right) + \bar{\Gamma}_{j0}^i \bar{h} u^j + \bar{\Gamma}_{jk}^i \bar{T}^{jk} \quad (\text{B.1})$$

eq:div2

Note that the total Jacobian \mathbf{J} comes from the composition of the spherical and of the ALE transformations, $\mathbf{J} = \mathbf{J}_A \mathbf{J}_F$ with determinant $J = J_A \sqrt{G}$. Moreover we have separated the Christoffel symbols related to time and space variation of the basis vectors.

The last step consists in transforming each $\{\bar{h} u^i, \bar{T}^{i1}, \bar{T}^{i2}\}$ into actual components $\{hu^i, T^{i1}, T^{i2}\}$ through the inverse Jacobian \mathbf{J}_A^{-1} (A.9)

$$\bar{h} u^i = hu^i \quad (\text{B.2})$$

$$\bar{T}^{ij} = \frac{\partial \chi^j}{\partial x^k} T^{ik} - \Sigma^j hu^i \quad (\text{B.3})$$

If we replace the transformed variables (B.3) into (B.1) we note that ALE terms related to Christoffel symbols cancel out. This leads to the ALE-SWEs in the reference parametric coordinates:

$$\frac{1}{J_A \sqrt{G}} \frac{\partial}{\partial t} \Big|_{\chi} \left(J_A \sqrt{G} hu^i \right) + \frac{1}{J_A \sqrt{G}} \frac{\partial}{\partial \chi^j} \left(J_A \sqrt{G} \frac{\partial \chi^j}{\partial x^k} T^{ik} - J_A \sqrt{G} \Sigma^j hu^i \right) + \bar{\Gamma}_{jk}^i \frac{\partial \chi^k}{\partial x^m} T^{jm} = 0 \quad (\text{B.4})$$

which appear in the same form of [18] except that momentum components are covariant and not physical.

To get the counterpart of (B.4) into actual components it suffices to apply chain rule to each term.

The advective term then reads

$$\begin{aligned} \frac{\partial}{\partial \chi^j} \left(J_A \sqrt{G} \frac{\partial \chi^j}{\partial x^k} T^{ik} \right) &= J_A \frac{\partial \chi^j}{\partial x^k} \frac{\partial}{\partial \chi^j} \left(\sqrt{G} T^{ik} \right) + \sqrt{G} T^{ik} \frac{\partial}{\partial \chi^j} \left(J_A \frac{\partial \chi^j}{\partial x^k} \right) \\ &= J_A \frac{\partial}{\partial x^k} \left(\sqrt{G} T^{ik} \right) \end{aligned} \quad (\text{B.5})$$

The second term on the right hand side is set to zero thanks to the metric identity. The ALE term goes similarly:

$$\begin{aligned} \frac{\partial}{\partial \chi^j} \left(J_A \sqrt{G} \Sigma^j hu^i \right) &= J_A \frac{\partial \chi^j}{\partial x^k} \frac{\partial}{\partial \chi^j} \left(\sqrt{G} \sigma^k hu^i \right) + \sqrt{G} \sigma^k hu^i \frac{\partial}{\partial \chi^j} \left(J_A \frac{\partial \chi^j}{\partial x^k} \right) \\ &= J_A \frac{\partial}{\partial x^k} \left(\sqrt{G} \sigma^k hu^i \right) \end{aligned} \quad (\text{B.6})$$

Replacing (B.5), (B.6) and (A.12) in (B.4) we get the ALE-SWEs on a 2D manifold with respect to the actual parametric coordinates:

$$\frac{\partial}{\partial t} \Big|_x \left(\sqrt{G} J_A h u^i \right) + J_A \frac{\partial}{\partial x^j} \left(\sqrt{G} T^{ij} - \sqrt{G} h u^i \sigma^j \right) + \sqrt{G} J_A \Gamma_{jk}^i T^{jk} = 0 \quad (\text{B.7})$$

521 Except for the physical source terms, the above set of equations coincides with (13) which is the momentum
 522 equation discretized in this article. In section 4 it has been obtained by a more classical procedure
 523 combining transport formulas and the GCL.

524

Appendix C. Proof of proposition 1

525
 app:a3

The validity of (34), (35) and (36) as a consequence of the constant definition (37) is trivially shown using (31) and the definition of the integrated edge velocities (32)-(33). Concerning the accuracy of the projection, we remark that by virtue of the mean value theorem

$$|\bar{\mathcal{K}}| = \int_{\bar{K}} \sqrt{G}(\bar{\mathbf{x}}) d\bar{\mathbf{x}} = |\bar{K}| \sqrt{G}(\bar{\mathbf{x}}_*) \rightarrow \int_{\bar{K}} (\sqrt{G}(\bar{\mathbf{x}}) - \sqrt{G}(\bar{\mathbf{x}}_*)) d\bar{\mathbf{x}} = 0 \quad (\text{C.1})$$

eq:relG

for some $\bar{\mathbf{x}}_*$ within the element. Estimating the error of (38) is equivalent to estimating the error of

$$\int_{\bar{K}} \varphi_i(\bar{\mathbf{x}}) f_h(\bar{\mathbf{x}}) \sqrt{G}(\bar{\mathbf{x}}) d\bar{\mathbf{x}} \approx \int_{\bar{K}} \varphi_i(\bar{\mathbf{x}}) f_h(\bar{\mathbf{x}}) \sqrt{G}(\bar{\mathbf{x}}_*) d\bar{\mathbf{x}}$$

To this end, we follow the consistency analysis used e.g. in [45, 44]: we take the difference between the two expressions, sum over all the elements, multiply by the sampled nodal values of an arbitrary test function $\psi \in C^r$ ($r \geq 1$), and sum over all the nodes. We end up with the following global error

$$\epsilon := \left| \sum_K \sum_{j \in K} \int_{\bar{K}} \psi_j \varphi_j(\bar{\mathbf{x}}) f_h(\bar{\mathbf{x}}) (\sqrt{G}(\bar{\mathbf{x}}) - \sqrt{G}(\bar{\mathbf{x}}_*)) d\bar{\mathbf{x}} \right| = \left| \sum_K \int_{\bar{K}} \psi_h(\bar{\mathbf{x}}) f_h(\bar{\mathbf{x}}) (\sqrt{G}(\bar{\mathbf{x}}) - \sqrt{G}(\bar{\mathbf{x}}_*)) d\bar{\mathbf{x}} \right|$$

The trick is now to use (C.1) to remove nodal values $\psi_j f_j$, leading to

$$\epsilon = \left| \sum_K \sum_{j \in K} \int_{\bar{K}} \frac{\psi_h(\bar{\mathbf{x}}) f_h(\bar{\mathbf{x}}) - \psi_j f_j}{3} (\sqrt{G}(\bar{\mathbf{x}}) - \sqrt{G}(\bar{\mathbf{x}}_*)) d\bar{\mathbf{x}} \right|$$

We now use the relation $(ab)_2 - (ab)_1 = (a_2 + a_1)(b_2 - b_1)/2 + (a_2 - a_1)(b_2 + b_1)/2$ and recast the error as

$$\epsilon = \left| \sum_K \sum_{j \in K} \int_{\bar{K}} \left(\frac{\psi_h + \psi_j}{6} (f_h(\bar{\mathbf{x}}) - f_j) + (\psi_h - \psi_j) \frac{f_h(\bar{\mathbf{x}}) + f_j}{6} \right) (\sqrt{G}(\bar{\mathbf{x}}) - \sqrt{G}(\bar{\mathbf{x}}_*)) d\bar{\mathbf{x}} \right|$$

We can now use standard arguments to bound this quantity as

$$\begin{aligned} \epsilon &\leq \sum_K \sum_{j \in K} \int_{\bar{K}} \left(\frac{|\psi_h + \psi_j|}{6} |f_h(\bar{\mathbf{x}}) - f_j| + |\psi_h - \psi_j| \frac{|f_h(\bar{\mathbf{x}}) + f_j|}{6} \right) |\sqrt{G}(\bar{\mathbf{x}}) - \sqrt{G}(\bar{\mathbf{x}}_*)| d\bar{\mathbf{x}} \\ &\leq c_1 |S^2| \left(\|\psi\|_{L^\infty} \sup_j \|\partial_{x^j} f\|_{L^\infty} + \sup_j \|\partial_{x^j} \psi\|_{L^\infty} \|f\|_{L^\infty} \right) \sup_j \|\partial_{x^j} \sqrt{G}\|_{L^\infty} h^2 \end{aligned}$$

526 **Appendix D. Stabilized FEM and RD in moving curvilinear coordinates**

app:a4

527 We sketch here the derivation of the predictor corrector scheme (50)-(58), and provide some details
 528 concerning the computation of the mass matrices with and without the simplified quadrature of proposition
 529 1.

530 We start with the following explicit unstabilized predictor:

$$\int_{S^2} \varphi_i \sqrt{G} J_A^{n+1} \mathbf{w}^* d\mathcal{X} - \int_{S^2} \varphi_i \sqrt{G} J_A^n \mathbf{w}^n d\mathcal{X} + \Delta t \int_{S^2} \varphi_i \bar{J}_A \left\{ \partial_{x^j} (\mathbf{F}^j - \sqrt{G} \sigma^j \mathbf{w})^n + \sqrt{G} S^n \right\} d\mathcal{X} = 0 \quad (\text{D.1}) \quad \text{eq:a1}$$

531 which we recast as

$$\begin{aligned} \int_{S^2} \varphi_i \sqrt{G} J_A^{n+1} (\mathbf{w}^* - \mathbf{w}^n) d\mathcal{X} + \Delta t \int_{S^2} \varphi_i \sqrt{G} \frac{J_A^{n+1} - J_A^n}{\Delta t} \mathbf{w}^n d\mathcal{X} \\ + \Delta t \int_{S^2} \varphi_i \bar{J}_A \left\{ \partial_{x^j} (\mathbf{F}^j - \sqrt{G} \sigma^j \mathbf{w})^n + \sqrt{G} S^n \right\} d\mathcal{X} = 0. \end{aligned} \quad (\text{D.2}) \quad \text{eq:a2}$$

532 For a fixed mesh, $J_A = 1$ and $\sigma^j = 0$. For a moving mesh (and only for a moving mesh) we assume
 533 that the mass matrices are computed following proposition 1. Otherwise, on fixed meshes we can either
 534 use the approximate quadrature of the proposition, or exact (or higher order) quadrature of (17), (21)
 535 and (22). In any case, either by cancellation, or by virtue of (36), we can recast the scheme as

$$\int_{S^2} \varphi_i \sqrt{G} J_A^{n+1} (\mathbf{w}^* - \mathbf{w}^n) d\mathcal{X} + \Delta t \int_{S^2} \varphi_i \bar{J}_A \left\{ \partial_{x^j} (\mathbf{F}^j)^n - \sqrt{G} \sigma^j \partial_{x^j} \mathbf{w}^n + \sqrt{G} S^n \right\} d\mathcal{X} = 0. \quad (\text{D.3}) \quad \text{eq:a3}$$

536 As in [33] we 1) stabilize the predictor step using an incomplete residual which does not involve the
 537 time increment, and 2) lump the Galerkin mass matrix to obtain:

$$\begin{aligned} \left(\sum_{K \ni i} \mathcal{K}_i \right) (\mathbf{w}_i^* - \mathbf{w}_i^n) + \Delta t \int_{S^2} \varphi_i \bar{J}_A \left\{ \partial_{x^j} (\mathbf{F}^j)^n - \sqrt{G} \sigma^j \partial_{x^j} \mathbf{w}^n + \sqrt{G} S^n \right\} d\mathcal{X} \\ + \Delta t \sum_{K \ni i} \int_{K_0} \gamma_i \bar{J}_A \left\{ \partial_{x^j} (\mathbf{F}^j)^n - \sqrt{G} \sigma^j \partial_{x^j} \mathbf{w}^n + \sqrt{G} S^n \right\} d\mathcal{X} = 0. \end{aligned} \quad (\text{D.4}) \quad \text{eq:a4}$$

538 where γ_i is a properly defined stabilization *bubble*. In particular, following [46, 33] it is assumed that for
 539 RD schemes the definition of the right hand side is such that

$$\int_{K_0} (\varphi_i + \gamma_i) \bar{J}_A \left\{ \partial_{x^j} (\mathbf{F}^j)^n - \sqrt{G} \sigma^j \partial_{x^j} \mathbf{w}^n + \sqrt{G} S^n \right\} d\mathcal{X} = \tilde{\Phi}_i^K$$

540 To recover [\(50\)](#) ^{[RC-pred](#)} we use the second in [\(38\)](#) ^{[eq:gal-mass-d](#)}, to replace the lumped mass matrix with $|\mathcal{C}_i|$.

The corrector step is derived in a similar manner. We start from the second stage Runge-Kutta iteration for the unstabilized Galerkin scheme:

$$\int_{S^2} \varphi_i \sqrt{G} J_A^{n+1} \mathbf{w}^{n+1} d\mathcal{X} - \int_{S^2} \varphi_i \sqrt{G} J_A^n \mathbf{w}^n d\mathcal{X} + \frac{\Delta t}{2} \int_{S^2} \varphi_i \bar{J}_A \left\{ \partial_{x^j} (\mathbf{F}^j - \sqrt{G} \sigma^j \mathbf{w})^n + \sqrt{G} \mathcal{S}^n \right\} d\mathcal{X} \\ + \frac{\Delta t}{2} \int_{S^2} \varphi_i \bar{J}_A \left\{ \partial_{x^j} (\mathbf{F}^j - \sqrt{G} \sigma^j \mathbf{w})^* + \sqrt{G} \mathcal{S}^* \right\} d\mathcal{X} = 0 \quad (\text{D.5}) \quad \boxed{\text{eq:a5}}$$

541 As proposed in [\[46, 33\]](#) ^{[RiA:10, ArR:14](#)}, we stabilize the scheme using the approximate *shifted* residual in which \mathbf{w}^{n+1}
542 is replaced by \mathbf{w}^* :

$$\int_{S^2} \varphi_i \sqrt{G} J_A^{n+1} \mathbf{w}^{n+1} d\mathcal{X} - \int_{S^2} \varphi_i \sqrt{G} J_A^n \mathbf{w}^n d\mathcal{X} + \frac{\Delta t}{2} \int_{S^2} \varphi_i \bar{J}_A \left\{ \partial_{x^j} (\mathbf{F}^j - \sqrt{G} \sigma^j \mathbf{w})^n + \sqrt{G} \mathcal{S}^n \right\} d\mathcal{X} \\ + \frac{\Delta t}{2} \int_{S^2} \varphi_i \bar{J}_A \left\{ \partial_{x^j} (\mathbf{F}^j - \sqrt{G} \sigma^j \mathbf{w})^* + \sqrt{G} \mathcal{S}^* \right\} d\mathcal{X} \\ + \sum_{K \ni i} \int_{K_0} \gamma_i \left\{ \sqrt{G} J_A^{n+1} \mathbf{w}^* - \sqrt{G} J_A^n \mathbf{w}^n + \frac{\Delta t}{2} \bar{J}_A \left[\partial_{x^j} (\mathbf{F}^j - \sqrt{G} \sigma^j \mathbf{w}) + \sqrt{G} \mathcal{S} \right]^n \right. \\ \left. + \frac{\Delta t}{2} \bar{J}_A \left[\partial_{x^j} (\mathbf{F}^j - \sqrt{G} \sigma^j \mathbf{w}) + \sqrt{G} \mathcal{S} \right]^* \right\} d\mathcal{X} = 0 \quad (\text{D.6}) \quad \boxed{\text{eq:a6}}$$

543 We now add and remove the term $\int_{S^2} \varphi_i \sqrt{G} J_A^{n+1} \mathbf{w}^* d\mathcal{X}$ to obtain the following error correction form
544 of the stabilized scheme [\[46\]](#) ^{[RiA:10](#)}

$$\int_{S^2} \varphi_i \sqrt{G} J_A^{n+1} (\mathbf{w}^{n+1} - \mathbf{w}^*) d\mathcal{X} = - \sum_{K \ni i} \int_{K_0} (\varphi_i + \gamma_i) \left\{ \sqrt{G} J_A^{n+1} \mathbf{w}^* - \sqrt{G} J_A^n \mathbf{w}^n \right. \\ \left. + \frac{\Delta t}{2} \bar{J}_A \left[\partial_{x^j} (\mathbf{F}^j - \sqrt{G} \sigma^j \mathbf{w}) + \sqrt{G} \mathcal{S} \right]^n \right. \\ \left. + \frac{\Delta t}{2} \bar{J}_A \left[\partial_{x^j} (\mathbf{F}^j - \sqrt{G} \sigma^j \mathbf{w}) + \sqrt{G} \mathcal{S} \right]^* \right\} d\mathcal{X} \quad (\text{D.7}) \quad \boxed{\text{eq:a7}}$$

545 For piecewise constant (per element) values of γ_i , we can see that in general the form of the full mass
546 matrix on a manifold is

$$m_{ij}^K = (m_{ij}^{GAL})^K + \mathcal{K}_j \gamma_i$$

547 If proposition 1 is valid, the last expression becomes

$$m_{ij}^K = |\mathcal{K}| \frac{\delta_{ij} + 1}{12} + \frac{|\mathcal{K}|}{3} \gamma_i$$

548 The standard RD mass matrix corrections are obtained by setting $\gamma_i = \beta_i^K - 1/3$, while the final form
549 [\(47\)](#) ^{[RC-corr](#)} of the scheme is obtained by recalling the hypothesis [\[46\]](#) ^{[RiA:10](#)}:

$$\Phi_i^K = \int_{K_0} (\varphi_i + \gamma_i) \left\{ \frac{\sqrt{G} J_A^{n+1} \mathbf{w}^* - \sqrt{G} J_A^n \mathbf{w}^n}{\Delta t} + \frac{1}{2} \bar{J}_A \left[\partial_{x^j} (\mathbf{F}^j - \sqrt{G} \sigma^j \mathbf{w}) + \sqrt{G} \mathcal{S} \right]^n + \frac{1}{2} \bar{J}_A \left[\partial_{x^j} (\mathbf{F}^j - \sqrt{G} \sigma^j \mathbf{w}) + \sqrt{G} \mathcal{S} \right]^* \right\} d\mathcal{X}$$

550

551 **References**

- ArR:1752** [1] L. Arpaia, M. Ricchiuto, r-adaptation for shallow water flows: conservation, well balancedness, efficiency, *Computers & Fluids* 160 (2018) 175–203.
553
- Ros:0454** [2] J. A. Rossmannith, D. S. Bale, R. J. LeVeque, A wave propagation algorithm for hyperbolic systems on curved manifold, *J. Comput. Phys.* 199 (2004) 631–662.
555
- Ros:0656** [3] J. A. Rossmannith, A wave propagation algorithm for hyperbolic systems the sphere, *J. Comput. Phys.* 213 (2006) 629–658.
557
- ULJ:1038** [4] P. A. Ullrich, C. Jablonowski, B. Van-Leer, High-order finite-volume methods for the shallow water equations on the sphere, *J. Comput. Phys.* 229 (2010) 6104–6134.
559
- Cas:1860** [5] M. Castro, S. Ortega, C. Parés, Well-balanced methods for the shallow water equations in spherical coordinates, *Computers & Fluids* 169 (2018) 129–140.
561
- Comb:0932** [6] R. Comblen, S. Legrand, E. Deleersnijder, V. Legat, A finite element method for solving the shallow water equations on the sphere, *Ocean Modelling* 28 (2009) 12–23.
563
- Bern:0934** [7] P. E. Bernard, J. F. Remacle, R. Comblen, V. Legat, K. Hillewaert, High-order discontinuous Galerkin schemes on general 2D manifolds applied to the shallow water equations, *J. Comput. Phys.* 228 (2009) 6514–6535.
565
566
- Ros:1337** [8] J. A. Rossmannith, Residual distribution schemes for hyperbolic balance laws in generalized coordinates, in: *Numerical Modeling of Space Plasma Flows*, Vol. 359 of ASP Conference Series, Nikolai V. Pogorelov and Gary P. Zank, 2013.
568
569
- RiB:0970** [9] M. Ricchiuto, A. Bollerman, Stabilized residual distribution for shallow water simulations, *J. Comput. Phys* 228 (2009) 1071–111.
571
- r1172** [10] M. Ricchiuto, On the C-property and generalized C-property of residual distribution for the shallow water equations, *J. Sci. Comput.* 48 (2011) 304–318.
573

- Ric:1574** [11] M. Ricchiuto, An explicit residual based approach for shallow water flows, *J. Comput. Phys.* 80 (2015) 306–344.
575
- SkK:9276** [12] W. Skamarock, J. Klemp, Adaptive grid refinement for two-dimensional and three-dimensional non-hydrostatic atmospheric flow, *Mon. Weather Rev.* 121 (1992) 788–804.
577
- McU:1578** [13] P. McCorquodale, P. Ullrich, H. Johansen, P. Colella, An adaptive multi-block high-order finite-volume method for solving the shallow water equations on the sphere, *Comm. App. Math. and Comp. Sci.* 10 (2) (2015) 121–162.
579
580
- Fer:168** [14] J. Ferguson, C. Jablonowski, H. Johansen, P. McCorquodale, P. Colellaand, P. Ullrich, Analyzing the adaptive mesh refinement (AMR) characteristics of a high-order 2D cubed-sphere shallow-water model, *Mon. Weather Rev.* 144 (12) (2016) 4641–4666.
582
583
- LGB:1184** [15] R. LeVeque, D. George, M. Berger, Tsunami modelling with adaptively refined finite volume methods, *Acta Numerica* 20 (2011) 211–289.
585
- Pop:1186** [16] S. Popinet, Quadtree-adaptive tsunami modelling, *Ocean Dynamics* 61 (9) (2011) 1261–1285.
- HIRT197422767** [17] C. W. Hirt, A. A. Amsden, J. L. Cook, An Arbitrary Lagrangian-Eulerian computing method for all flow speeds, *J. Comput. Phys.* 14 (3) (1974) 227–253.
588
- PS:0389** [18] J. Prusa, P. Smolarkiewicz, An all-scale anelastic model for geophysical flows: dynamic grid deformation, *J. Comp. Phys.* 190 (2003) 601–622.
590
- KSD:1291** [19] C. Kuhnlein, P. Smolarkiewicz, A. Dornbrack, Modelling atmospheric flows with adaptive moving meshes, *J. Comp. Phys.* 231 (2012) 2741–2763.
592
- Zho:1393** [20] F. Zhou, G. Chen, Y. Huang, J. Z. Yang, H. Feng, An adaptive moving finite volume scheme for modeling flood inundation over dry and complex topography, *Water Resour. Res.* 49 (2013) 1914–1928.
594
595
- Ba0896** [21] Y. Bazilevs, V. M. Calo, T. J. R. Hughes, Y. Zhang, Isogeometric fluid-structure interaction: theory, algorithms, and computations, *Comput. Mech.* 43 (2008) 3–37.
597
- CFSI1298** [22] Y. Bazilevs, K. Takizawa, T. F. Tezduyar, Computational Fluid-Structure Interaction. Methods and applications, Wiley, 2012.
599
- D1200** [23] V. A. Dobrev, T. V. Kolev, R. N. Rieben, High-order curvilinear finite element methods for Lagrangian hydrodynamics, *SIAM J. Sci. Comput.* 34 (2012) B606–B641.
601

- BOSCHERI20164803** [24] W. Boscheri, M. Dumbser, High order accurate direct Arbitrary-Lagrangian-Eulerian ADER-WENO
603 finite volume schemes on moving curvilinear unstructured meshes, *Computers & Fluids* 136 (2016)
604 48 – 66.
- BOSCHERI201448403** [25] W. Boscheri, M. Dumbser, A direct Arbitrary Lagrangian Eulerian ADER-WENO finite volume
606 scheme on unstructured tetrahedral meshes for conservative and non-conservative hyperbolic systems
607 in 3D, *J. Comput. Phys.* 275 (2014) 484 – 523.
- VILAR201418803** [26] F. Vilar, P.-H. Maire, R. Abgrall, A discontinuous Galerkin discretization for solving the two-
609 dimensional gas dynamics equations written under total Lagrangian formulation on general unstruc-
610 tured grids, *J. Comput. Phys.* 276 (2014) 188 – 234.
- t161** [27] S. A. Teukolsky, Formulation of discontinuous Galerkin methods for relativistic astrophysics, *J. Com-
612 put. Phys.* 312 (2016) 333–356.
- ThL:7913** [28] P. Thomas, C. Lombard, Geometric conservation law and its application to flow computations on
614 moving grids, *AIAA Journal* (1979) 1030–1037.
- LeF:9613** [29] M. Lesoinne, C. Farhat, Geometric conservation laws for flow problems with moving boundaries and
616 deformable meshes, and their impact on aeroelastic computations, *Comput. Meth. Appl. Mech. Engrg*
617 134 (1996) 71–90.
- GuF:0013** [30] H. Guillard, C. Farhat, On the significance of the geometric conservation law for flow computations
619 on moving meshes, *Comput. Meth. Appl. Mech. Engrg* 190 (2000) 1467–1482.
- Eti:0920** [31] S. Etienne, A. Garon, D. Pelletier, Geometric conservation law and finite element methods for 3D
621 unsteady simulations of incompressible flow, in: *39th AIAA Fluid Dynamics Conference, 22-25 June*
622 *2009. San Antonio, Texas, 2009.*
- SaA:0823** [32] S. Savidis, D. Aubram, F. Rackwit, Arbitrary Lagrangian Eulerian finite element formulation for
624 geotechnical construction processes, *Journal of Theoretical and Applied Mechanics* 38 (2008) 165–
625 174.
- ArR:1423** [33] L. Arpaia, M. Ricchiuto, R. Abgrall, An ALE formulation for explicit Runge-Kutta residual distri-
627 bution, *J. Sci. Comput.* 190 (34) (2014) 1467–1482.
- Lev:9723** [34] R. LeVeque, Wave propagation algorithm for multidimensional hyperbolic systems, *J. Comput. Phys.*
629 131 (1997) 3279–353.

- Tru:630** [35] C. Truesdell, The mechanical foundations of elasticity and fluid dynamics, Gordon and Breach Science
631 Publicher Inc., 1966.
- Wil:073** [36] D. Williamson, The evolution of dynamical cores for global atmospheric models, *J. Meteorol. Soc.*
633 *Jpn.* 85 (2007) 241–269.
- KaS:043** [37] A. Kageyama, T. Sato, "Yin-Yang grid": An overset grid in spherical geometry, *Geochem. Geophys.*
635 *Geosyst.* 5 (2004) Q09005.
- RoI:963** [38] C. Ronchi, R. Iacono, P. S. Paolucci, The "cubed sphere": A new method for the solution of partial
637 differential equations in spherical geometry, *J. Comput. Phys.* 124 (1996) 93–114.
- BeV:943** [39] A. Bermudez, M. E. Vazquez-Cendon, Upwind methods for hyperbolic conservation laws with source
639 terms, *Comput. Fluids* 235 (8) (1994) 1049–1071.
- ZhC:134** [40] F. Zhou, G. Chen, S. Noelle, H. Guo, A well-balanced stable GRP scheme for shallow water equations
641 for adaptive unstructured triangular meshes, *Int. J. Numer. Meth. Fl.* 73 (2013) 266–283.
- Ngu:144** [41] H. Nguyen-Shafer, J.-P. Schmidh, *Tensor Analysis and Elementary Differential Geometry for Physi-*
643 *cist and Engineers*, Vol. 21 of *Mathematical Engineering*, Springer, 2014.
- MaY:064** [42] D. J. Mavriplis, Z. Yang, Construction of the discrete geometric conservation law for high-order
645 time-accurate simulations on dynamic meshes, *J. Comput. Phys.* 213 (2006) 557–573.
- shoelac04** [43] B. Braden, The surveyor's area formula, *The College Mathematics Journal* 17 (4) (1986) 326–337.
- Dec:174** [44] H. Deconinck, M. Ricchiuto, Residual distribution schemes: Foundations and analysis, in: J. Wiley,
648 Sons (Eds.), *Encyclopedia of Computational Mechanics*, second edition, 2017.
- AR:174** [45] R. Abgrall, M. Ricchiuto, High order methods for CFD, in: R. d. B. Erwin Stein, T. J. Hughes (Eds.),
650 *Encyclopedia of Computational Mechanics*, Second Edition, John Wiley and Sons, 2017.
- RiA:103** [46] M. Ricchiuto, R. Abgrall, Explicit Runge-Kutta residual distribution schemes for time dependent
652 problems: Second order case, *J. Comput. Phys.* 229 (16) (2010) 5653–5691.
- hr143** [47] M. Hubbard, M. Ricchiuto, Discontinuous upwind residual distribution: A route to unconditional
654 positivity and high order accuracy, *Computers & Fluids* 46 (1) (2011) 263 – 269.
- shr133** [48] D. Sármany, M. Hubbard, M. Ricchiuto, Unconditionally stable space-time discontinuous residual
656 distribution for shallow-water flows, *Journal of Computational Physics* 253 (2013) 86 – 113.

- hrs2067** [49] M. Hubbard, M. Ricchiuto, D. Sármany, Space-time residual distribution on moving meshes, *Computers & Mathematics with Applications* doi:<https://doi.org/10.1016/j.camwa.2019.09.019>.
658
- Abg:069** [50] R. Abgrall, Essentially non-oscillatory residual distribution schemes for hyperbolic problems, *J. Comput. Phys.* 214 (2006) 773–808.
660
- DeB:736** [51] C. de Boor, *Good Approximations by Splines with Variable Knots II*, Vol. 363, Springer, Berlin, 1973.
- CeH:046** [52] H. Ceniceros, T. Hou, An efficient dynamically adaptive mesh for potentially singular solutions, *J. Comput. Phys.* 172 (2001) 609–639.
663
- TaT:036** [53] H. Tang, T. Tang, Adaptive mesh methods for one and two-dimensional hyperbolic conservation laws, *SIAM J. Numer. Anal.* 41 (2) (2003) 487–515.
665
- JIN200668** [54] C. Jin, K. Xu, An adaptive grid method for two-dimensional viscous flows, *J. Comput. Phys.* 218 (1) (2006) 68 – 81.
667
- ChT:088** [55] G. Chen, H. Tang, P. Zhang, Second-order accurate Godunov scheme for multicomponent flows on moving triangular meshes, *J. Sci. Comput.* 34 (2008) 64–86.
669
- XuN:137** [56] G. Ni, S. Jiang, K. Xu, Remapping-free ALE-type kinetic method for flow computations, *J. Comp. Phys.* 228 (2009) 3154–3171.
671
- PAN2015207** [57] L. Pan, K. Xu, Generalized coordinate transformation and gas-kinetic scheme, *J. Comput. Phys.* 287 (2015) 207 – 225.
673
- WeB:167** [58] H. Weller, P. Browne, C. Budd, M. Cullen, Mesh adaptation on the sphere using optimal transport and the numerical solution of a Monge-Ampere type equation, *J. Comput. Phys.* 308 (2016) 102–123.
675
- McR:187** [59] A. McRae, C. Cotter, C. Budd, Optimal-transport-based mesh adaptivity on the plane and sphere using finite elements, *SIAM J. Sci. Comp.* 40 (2) (2018) A1121–A1148.
677
- DiL:067** [60] Y. Di, R. Li, T. Tang, P. Zhang, Moving mesh methods for singular problems on a sphere using perturbed harmonic mappings, *J. Sci. Comput.* 28 (4) (2006) 1490–1508.
679
- HuR:976** [61] W. Huang, R. D. Russell, Analysis of moving mesh partial differential equations with spatial smoothing, *J. Numer. Anal.* 34 (3) (1997) 1106–1126.
681
- BuH:098** [62] C. J. Budd, W. Huang, R. D. Russell, *Adaptivity with moving grids*, Cambridge University Press, 2009, Ch. 1, pp. 1–131.
683

- Win:6764** [63] A. M. Winslow, Numerical solution of the quasi-linear Poisson equation, *J. Comput. Phys.* 1 (1967) 149–172.
685
- GuR:9786** [64] C. Geuzaine, J.-F. Remacle, Gmsh: a three-dimensional finite element mesh generator with built-in pre- and post-processing facilities, <http://www.geuz.org/gmsh> (1997-2017).
687
- Wil:9288** [65] D. L. Williamson, J. B. Drake, J. J. Hack, R. Jakob, P. N. Swarztrauber, A standard test set for numerical approximations to the shallow water equations in spherical geometry, *J. Comput. Phys.* 102 (1992) 211–224.
689
690
- Gal:0461** [66] J. Galewsky, R. Scott, L. Polvani, An initial-value problem for testing numerical models of the global shallow-water equations, *Tellus A: Dynamic Meteorology and Oceanography* (56:5) (2004) 429–440.
692
- brgm:1793** [67] S. LeRoy, A. Lemoine, R. Pedreros, M. Rousseau, Tohoku-Oki 2011 tsunami high-resolution modeling and sensitivity to the rupture complexity: Kamaishi and Sendai areas, in: TANDEM Workshop on French Japanese week on disaster risk reduction, Oct 2017, Tokyo, Japan, 2017.
694
695
- SaF:1396** [68] K. Satake, Y. Fujii, T. Harada, Y. Namegaya, Time and space distribution of coseismic slip of the 2011 tohoku earthquake as inferred from tsunami waveform data, *Bull. Seismol. Soc. Am.* 103 (2013) 1473–1492.
697
698
- Gal:1099** [69] G. Gayer, S. Leschka, I. Nohren, O. Larsen, H. Gunther, Unconditionally stable spacetime discontinuous residual distribution for shallow-water flows, *Nat. Hazards Earth Syst. Sci.* 10 (2010) 1679–1687.
700
- Che:1461** [70] C. Chen, Z. Lai, R. Beardsley, J. Sasaki, J. Lin, H. Lin, R. Ji, Y. Sun, The March 11, 2011 tohoku M9.0 earthquake-induced tsunami and coastal inundation along the Japanese coast: A model assessment, *Prog. Oceanogr.* 123 (2014) 84–104.
702
703
- LoK:1264** [71] F. Loevholt, G. Kaiser, S. Glimsdal, L. Scheele, C. Harbitz, , G. Pedersen, Modeling propagation and inundation of the 11 March 2011 Tohoku tsunami, *Nat. Hazards Earth Syst. Sci.* 12 (2012) 1017–1028.
705
- ShS:1266** [72] T. Shimozono, S. Sato, A. Okayasu, Y. Tajima, H. Fritz, , H. Liu, T. Takagawa, Propagation and inundation characteristics of the 2011 Tohoku tsunami on the central Sanriku coast, *Coast. Eng. J.* 54 (2012) 1017–1028.
707
708